

# Heatmap Regression via Randomized Rounding

Baosheng Yu, *Member, IEEE*, and Dacheng Tao, *Fellow, IEEE*

**Abstract**—Heatmap regression has become the mainstream methodology for deep learning-based semantic landmark localization, including in facial landmark localization and human pose estimation. Though heatmap regression is robust to large variations in pose, illumination, and occlusion in unconstrained settings, it usually suffers from a sub-pixel localization problem. Specifically, considering that the activation point indices in heatmaps are always integers, quantization error thus appears when using heatmaps as the representation of numerical coordinates. Previous methods to overcome the sub-pixel localization problem usually rely on high-resolution heatmaps. As a result, there is always a trade-off between achieving localization accuracy and computational cost, where the computational complexity of heatmap regression depends on the heatmap resolution in a quadratic manner. In this paper, we formally analyze the quantization error of vanilla heatmap regression and propose a simple yet effective quantization system to address the sub-pixel localization problem. The proposed quantization system induced by the *randomized rounding operation* 1) encodes the fractional part of numerical coordinates into the ground truth heatmap using a probabilistic approach during training; and 2) decodes the predicted numerical coordinates from a set of activation points during testing. We prove that the proposed quantization system for heatmap regression is unbiased and lossless. Experimental results on four popular facial landmark localization datasets (WFLW, 300W, COFW, and AFLW) demonstrate the effectiveness of the proposed method for efficient and accurate semantic landmark localization. Code is available at <http://github.com/baoshengyu/H3R>.

**Index Terms**—Semantic landmark localization, heatmap regression, quantization error, randomized rounding.

## 1 INTRODUCTION

SEMANTIC landmarks are sets of points or pixels in images containing rich semantic information. They reflect the intrinsic structure or shape of objects such as human faces [1], [2], hands [3], [4], bodies [5], [6], and household objects [7]. Semantic landmark localization is fundamental in computer and robot vision [8], [9], [7], [10]. For example, semantic landmark localization can be used to register correspondences between spatial positions and semantics (semantic alignment), which is extremely useful in many visual recognition tasks such as face recognition [8], [11] and person re-identification [12], [13]. Therefore, robust and efficient semantic landmark localization is extremely important in applications requiring the accurate positions of semantic landmarks including robotic grasping [7], [10] and a variety of facial analysis applications such as face makeup [14], [15], animation [16], [17], and reenactment [18], [9].

Coordinate regression and heatmap regression are two widely-used methods for deep learning-based semantic landmark localization [1], [19]. Rather than directly regressing the numerical coordinate with a fully-connected layer, heatmap-based methods aim to predict the heatmap in which the maximum activation point corresponds to the semantic landmark in the input image. Due to the effective spatial generalization of heatmap representations, heatmap regression is robust to large variations in pose, illumination, and occlusion in unconstrained settings [19], [20]. Heatmap regression has performed particularly well in a variety of semantic landmark localization tasks including facial landmark detection [2], [21] and human pose estimation [6], [22]. Despite this promise, using heatmap representation for

semantic landmark localization has an inherent drawback, namely that the indices of the activation points in heatmaps are always integers. Vanilla heatmap-based methods therefore fail to predict the numerical coordinates with sub-pixel precision. Sub-pixel localization is nevertheless important in many real-world scenarios, with the fractional part of numerical coordinates originating from: 1) the input image being captured either by a low-resolution camera and/or at a relatively large distance; and 2) the heatmap is usually at a much lower resolution than the input image due to the downsampling stride of convolutional neural networks. As a result, low-resolution heatmaps significantly degrade heatmap regression performance. Considering that the computational cost of deep neural networks usually depends quadratically on the resolution of the input image or the feature map, there is a trade-off between the localization accuracy and the computational cost for heatmap regression [6], [23], [24], [25], [26].

In vanilla heatmap regression, 1) during training, the ground truth numerical coordinates are first quantized to generate the ground truth heatmap; and 2) during testing, the predicted numerical coordinates can be decoded from the maximum activation point in the predicted heatmap. However, typical integer quantization operations used in vanilla heatmap regression such as **floor**, **round**, and **ceil** discard the fractional part of the ground truth numerical coordinates, making it difficult to reconstruct the fractional part even from the optimal predicted heatmap. This error induced by the transformation from the numerical coordinates to the heatmap is known as the quantization error. To address the problem of quantization error in heatmap regression, here we introduce a new quantization system to form a lossless transformation between the numerical coordinates and the heatmap. In our approach, during training, the proposed quantization system uses a set of activation

- Baosheng Yu and Dacheng Tao are with The University of Sydney, 6 Cleveland St, Darlington, NSW 2008, Australia.  
E-mail: {baosheng.yu, dacheng.tao}@sydney.edu.au

Manuscript received April 19, 2005; revised August 26, 2015.

points, and the fractional part of a numerical coordinate is encoded as the activation probability of a different activation point. During testing, the fractional part can then be reconstructed according to the activation probabilities of the top  $k$  maximum activation points in the predicted heatmap. To achieve this, we introduce a new quantization operation called randomized rounding, or **random-round**, which has been widely used in combinatorial optimization to convert fractional solutions into integer solutions with provable approximation guarantees [27], [28]. Furthermore, the proposed quantization system can easily be implemented using a few lines of source code in most deep learning packages, making it a plug-and-play replacement for the quantization system used in heatmap-based semantic landmark localization applications.

In this paper, we address the problem of quantization error in heatmap regression with a new quantization system. The remainder of the paper is structured as follows. In the preliminaries, we briefly review two typical semantic landmark localization methods, coordinate regression and heatmap regression. In the methods, we first describe sub-pixel localization and formally introduce the problem of quantization error by decomposing the prediction error into the heatmap error and the quantization error. We then discuss quantization bias in vanilla heatmap regression and prove a tight upper bound on the quantization error in vanilla heatmap regression. To address quantization error, we devise a new quantization system and theoretically prove that the proposed quantization system is unbiased and lossless. We also discuss uncertainty in heatmap prediction as well as the influence of unbiased human annotation when forming a robust semantic landmark localization system. In the experimental section, we demonstrate state-of-the-art performance of our proposed method on four popular facial landmark detection datasets, WFLW, 300W, COFW, and AFLW, based on a simple yet effective baseline model.

## 2 RELATED WORK

Semantic landmark localization, which aims to predict the numerical coordinates for a set of pre-defined semantic landmarks in a given image or video, has a variety of applications in computer and robot vision including facial landmark detection [1], [29], [2], hand landmark detection [3], [4], human pose estimation [5], [6], [22], and household object pose estimation [7], [10]. In this section, we briefly review recent works on coordinate regression and heatmap regression for semantic landmark localization, especially in facial landmark localization applications.

### 2.1 Coordinate Regression

Coordinate regression has been widely and successfully used in facial landmark localization under constrained settings, where it usually relies on simple yet effective features [30], [31], [32], [33]. To improve the performance of coordinate regression for facial landmark localization in the wild, several methods have been proposed by using cascade refinement [1], [34], [35], [36], parametric/non-parametric shape models [37], [29], [36], [38], multi-task learning [39], [40], [41], and novel loss functions [42], [43].

### 2.2 Heatmap Regression

The success of deep learning has prompted the use of heatmap regression for semantic landmark localization, especially for robust and accurate facial landmark localization [2], [44], [45], [23] and human pose estimation [19], [46], [6]. Existing heatmap regression methods either rely on large input images or empirical compensations during inference to mitigate the problem of quantization error [6], [47], [48], [22]. For example, a simple yet effective compensation method known as “shift a quarter to the second maximum activation point” has been widely used in many state-of-the-art heatmap regression methods [6], [49], [22].

Several methods have been developed to address the problem of quantization error, which can be divided into three main categories: 1) jointly predicting the heatmap and the offset in a multi-task manner [50]; 2) encoding and decoding the fractional part of numerical coordinates via a modulated 2D Gaussian distribution [24], [26]; and 3) exploring differentiable transformations between the heatmap and the numerical coordinates [51], [20], [52], [53]. Specifically, [24] generates the fractional part sensitive ground truth heatmap for video-based face alignment, which is known as fractional heatmap regression. Under the assumption that the predicted heatmap follows a 2D Gaussian distribution, [26] decodes the fractional part of numerical coordinates from the modulated predicted heatmap. The soft-argmax operation is differentiable [54], [55], [56], [53], and has been intensively explored in human pose estimation [51], [20].

## 3 PRELIMINARIES

In this section, we introduce two widely-used semantic landmark localization methods, coordinate regression and heatmap regression. For simplicity, we use facial landmark detection as an intuitive example to illustrate semantic landmark localization.

**Coordinate Regression.** Given a face image, semantic landmark detection aims to find the numerical coordinates of a set of pre-defined facial landmarks  $\mathbf{x}_i = (x_i, y_i)$ , where  $i = 1, 2, \dots, K$ , indicate the indices of different facial landmarks (e.g., a set of five pre-defined facial landmarks can be left eye, right eye, nose, left mouth corner, and right mouth corner). It is natural to train a model (e.g., deep neural networks) to directly regress the numerical coordinates of all facial landmarks. The coordinate regression model then can be optimized via a typical regression criterion such as mean squared error (MSE) and mean absolute error (MAE). For the MSE criterion (also the L2 loss), we have

$$\mathcal{L}(\mathbf{x}_i^p, \mathbf{x}_i^g) = \|\mathbf{x}_i^p - \mathbf{x}_i^g\|_2^2, \quad (1)$$

where  $\mathbf{x}_i^p$  and  $\mathbf{x}_i^g$  indicate the predicted and the ground truth numerical coordinates, respectively. When using the MAE criterion (also the L1 loss), the loss function  $\mathcal{L}$  can be defined in a similar way to (1).

**Heatmap Regression.** Heatmaps (also known as confidence maps) are simple yet effective representations of semantic landmark locations. Given the numerical coordinate  $\mathbf{x}_i$  for the  $i$ -th semantic landmark, it then corresponds to a specific heatmap  $\mathbf{h}_i$  as shown in Fig. 1. For simplicity, we assume  $\mathbf{h}_i$  is the same size as the input image in this

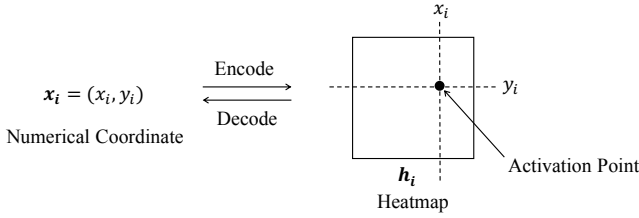


Fig. 1. An intuitive example of the heatmap representation for the numerical coordinate. Given the numerical coordinate  $\mathbf{x}_i = (x_i, y_i)$ , we then have the corresponding heatmap  $\mathbf{h}_i$  with the maximum activation point located at the position  $(x_i, y_i)$ . Above two representations are equivalent under the condition that  $(x_i, y_i) \in \mathbb{N}^2$ .

section and leave the problem of quantization error to the next section. With the heatmap representation, the problem of semantic landmark localization can be translated into heatmap regression via two heatmap subroutines: 1) **encode** (from the ground truth numerical coordinate  $\mathbf{x}_i^g$  to the ground-truth heatmap  $\mathbf{h}_i^g$ ); and 2) **decode** (from the predicted heatmap  $\mathbf{h}_i^p$  to the predicted numerical coordinate  $\mathbf{x}_i^p$ ). The main deep learning-based heatmap regression for semantic landmark localization framework is shown in Fig. 2. Specifically, during the inference stage, given a predicted heatmap  $\mathbf{h}_i^p$ , the value  $\mathbf{h}_i^p(\mathbf{x}) \in [0, 1]$  indicates the confidence score that the  $i$ -th landmark is located at coordinate  $\mathbf{x} \in \mathbb{N}^2$ . Then, we can decode the predicted numerical coordinate  $\mathbf{x}_i^p$  from the predicted heatmap  $\mathbf{h}_i^p$  using the **argmax** operation, i.e.,

$$\mathbf{x}_i^p = (x_i^p, y_i^p) \in \arg \max_{\mathbf{x}} \{\mathbf{h}_i^p(\mathbf{x})\}. \quad (2)$$

Therefore, with the decode operation in (2), the problem of semantic landmark localization can be solved by training a deep model to predict heatmap  $\mathbf{h}_i^p$ .

To train a heatmap regression model, the ground truth heatmap  $\mathbf{h}_i^g$  is indispensable, i.e., we need to encode the ground truth coordinate  $\mathbf{x}_i^g$  into the ground truth heatmap  $\mathbf{h}_i^g$ . We introduce two widely-used methods to generate the ground truth heatmap, **Gaussian heatmap** and **binary heatmap**, as follows. Given the ground truth coordinate  $\mathbf{x}_i^g$ , the ground truth Gaussian heatmap can be generated by sampling and normalizing from a bivariate normal distribution  $\mathcal{N}(\mathbf{x}_i^g, \Sigma)$ , i.e., the ground truth heatmap  $\mathbf{h}_i^g$  at location  $\mathbf{x} \in \mathbb{N}^2$  can be evaluated as

$$\mathbf{h}_i^g(\mathbf{x}) = \exp\left(-\frac{1}{2}(\mathbf{x} - \mathbf{x}_i^g)^\top \Sigma^{-1}(\mathbf{x} - \mathbf{x}_i^g)\right), \quad (3)$$

where  $\Sigma$  is the covariance matrix (a positive semi-definite matrix) and  $\sigma > 0$  is the standard deviation in both directions, i.e.,

$$\Sigma = \begin{bmatrix} \sigma^2 & 0 \\ 0 & \sigma^2 \end{bmatrix}. \quad (4)$$

When  $\sigma \rightarrow 0$ , the ground truth heatmap can be generated by assigning a positive value at the ground truth numerical coordinate  $\mathbf{x}_i^g$ , i.e.,

$$\mathbf{h}_i^g(\mathbf{x}) = \begin{cases} 1 & \text{if } \mathbf{x} = \mathbf{x}_i^g, \\ 0 & \text{otherwise.} \end{cases} \quad (5)$$

Specifically, when  $\sigma \rightarrow 0$ , the ground truth heatmap defined in (5) is also known as the **binary heatmap**. We demonstrate the ground truth heatmap generated by different  $\sigma$  in Fig. 3.

Given the ground truth heatmap, the heatmap regression model then can be optimized using typical pixel-wise regression criteria such as MSE, MAE, or Smooth-L1 [42]. Specifically, for Gaussian heatmaps, the heatmap regression model is usually optimized with the pixel-wise MSE criterion, i.e.,

$$\mathcal{L}(\mathbf{h}_i^p, \mathbf{h}_i^g) = \mathbb{E} \|\mathbf{h}_i^p(\mathbf{x}) - \mathbf{h}_i^g(\mathbf{x})\|_2^2. \quad (6)$$

When using the MAE/Smooth-L1 criteria, the loss function can be defined in a similar way to (6). For binary heatmap, the heatmap regression model can also be optimized with the pixel-wise cross-entropy criterion, i.e.,

$$\mathcal{L}(\mathbf{h}_i^p, \mathbf{h}_i^g) = \mathbb{E} (\mathcal{L}_{\text{CE}}(\mathbf{h}_i^p(\mathbf{x}), \mathbf{h}_i^g(\mathbf{x}))), \quad (7)$$

where  $\mathcal{L}_{\text{CE}}$  indicates the cross-entropy criterion with a softmax function as the activation/normalization function. A comprehensive review of different loss functions for semantic landmark localization is beyond the scope of this paper, but we refer interested readers to [43] for descriptions of coordinate regression and [21] for heatmap regression. Unless otherwise mentioned, we use the MSE criterion for Gaussian heatmap and the cross-entropy criterion for binary heatmap in this paper.

## 4 METHOD

In this section, we first introduce sub-pixel localization. We then formulate the quantization error in a unified way by correcting quantization bias in a vanilla quantization system. We then devise a new quantization system via randomized rounding to address the problem of quantization error in heatmap regression.

### 4.1 Sub-pixel Localization

Heatmaps are an effective representation of integer coordinates, but sub-pixel localization is common in real-world applications. Apart from occurring in images captured by low-resolution camera sensors, the problem of sub-pixel numerical coordinates usually applies when 1) the original image is resized during training and/or testing, i.e., the input image usually needs to be cropped from the original image and then resized according to the input size of the heatmap regression model; and 2) the feature maps of CNNs are usually downsampled to reduce the computational complexity. Specifically, the computational cost of CNNs depends on the resolution of the input image and the feature maps in a quadratic manner. As a result, there is always a trade-off between the localization accuracy and the computational cost in different applications. For example, with an input resolution of  $128 \times 128$  pixels and a downsampling stride of the feature map  $s = 4$ , the size of feature map will be  $32 \times 32$  pixels, which achieves a practically useful trade-off between the localization accuracy and the computational cost in real-world facial landmark detection applications.

Given the original input images of different resolutions, the downsampling stride of the heatmap is not always equal to the downsampling stride of the feature map. For example, given an original image of  $512 \times 512$  pixels, the

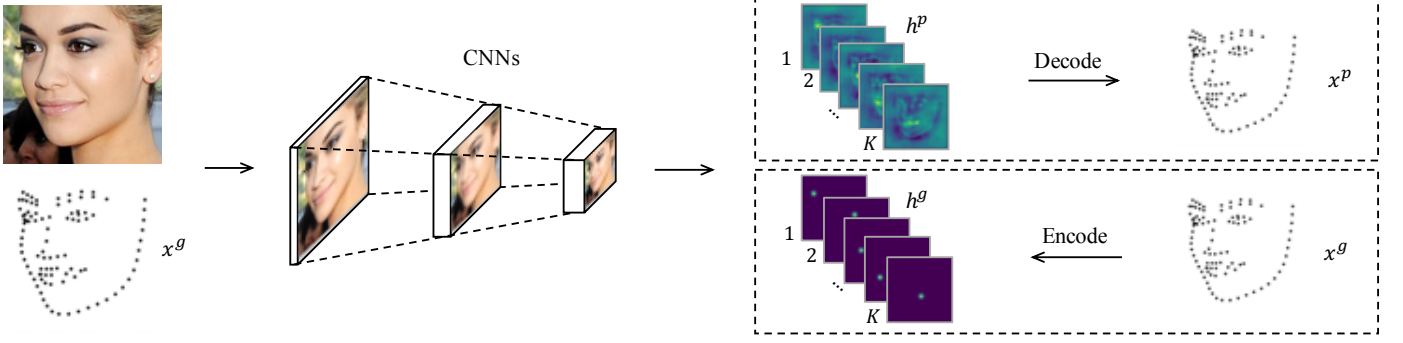


Fig. 2. The main deep learning-based heatmap regression for semantic landmark localization framework. Specifically, during the inference stage, we decode the predicted heatmaps  $\mathbf{h}^p = (\mathbf{h}_1^p, \dots, \mathbf{h}_K^p)$  to obtain the predicted numerical coordinates  $\mathbf{x}^p = (\mathbf{x}_1^p, \dots, \mathbf{x}_K^p)$ ; During the training stage, we encode the ground truth numerical coordinates  $\mathbf{x}^g = (\mathbf{x}_1^g, \dots, \mathbf{x}_K^g)$  to generate the ground truth heatmaps  $\mathbf{h}^g = (\mathbf{h}_1^g, \dots, \mathbf{h}_K^g)$  used as the supervision for training the heatmap regression model.

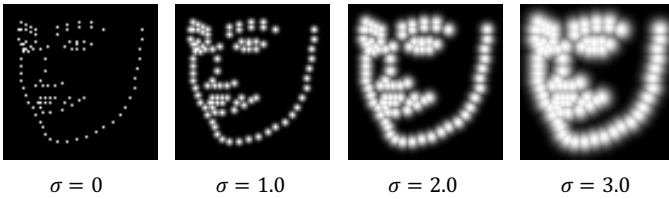


Fig. 3. An intuitive example of the ground truth heatmap with different  $\sigma$ . We plot all heatmaps  $\mathbf{h}_1^g, \dots, \mathbf{h}_{98}^g$  into a single figure for better visualization.

input size of a heatmap regression model  $128 \times 128$  pixels, and a downsampling stride of the feature map of 4 pixels, we then have a downsampling stride of the heatmap  $s = 512/(128/4) = 16$  pixels. For simplicity, we usually do not distinguish between the above two sub-pixel localization settings to formulate the quantization error in a unified manner. Unless otherwise mentioned, we refer to a downsampling stride  $s > 1$  as the downsampling stride of the heatmap.

## 4.2 Quantization System

Heatmap regression for semantic landmark localization usually contains two key components: 1) heatmap prediction; and 2) transformation between the heatmap and the numerical coordinates. The **quantization system** in heatmap regression is a combination of the **encode** and **decode** operations. Though heatmap regression has been successful for semantic landmark localization, it suffers from the inherent drawback of not being able to encode the fractional part of the numerical coordinates. Specifically, the numerical coordinate corresponds to the indices of a pixel in the heatmap, which are always integers. As a result, during training, the ground truth numerical coordinates  $\mathbf{x}_i^g$  will be quantized into integers before generating the ground truth heatmap. During the inference stage, the predicted numerical coordinates  $\mathbf{x}_i^p$  obtained by a decode operation in (2) are also integers. That is, heatmap regression usually fails to address the fractional part of the numerical coordinate during both training and inference, resulting in localization error.

To analyze the localization error caused by the quantization system in heatmap regression, we formulate the localization error as the sum of **heatmap error** and **quantization error** as follows:

$$\begin{aligned} \mathcal{E}_{loc} &= \|\mathbf{x}_i^p - \mathbf{x}_i^g\|_2 = \|\mathbf{x}_i^p - \mathbf{x}_i^{opt} + \mathbf{x}_i^{opt} - \mathbf{x}_i^g\|_2 \\ &\leq \underbrace{\|\mathbf{x}_i^p - \mathbf{x}_i^{opt}\|_2}_{\text{heatmap error}} + \underbrace{\|\mathbf{x}_i^{opt} - \mathbf{x}_i^g\|_2}_{\text{quantization error}}, \end{aligned} \quad (8)$$

where  $\mathbf{x}_i^{opt}$  indicates the numerical coordinate decoded from the optimal predicted heatmap. Generally, the heatmap error corresponds to the error in heatmap prediction, i.e.,  $\|\mathbf{h}_i^p - \mathbf{h}_i^g\|_2$ , and the quantization error indicates the error caused by both the encode and decode operations. If there is no heatmap error, the localization error then all originates from the error of the quantization system, i.e.,

$$\mathcal{E}_{loc} = \|\mathbf{x}_i^p - \mathbf{x}_i^g\|_2 = \|\mathbf{x}_i^{opt} - \mathbf{x}_i^g\|_2. \quad (9)$$

The generalizability of deep neural networks for heatmap prediction, i.e., the heatmap error, is beyond the scope of this paper. We do not consider the heatmap error during the analysis of quantization error in this paper.

To obtain integer coordinates for the generation of the ground truth heatmap, typical integer quantization operations such as **floor**, **round**, and **ceil** have been widely used in previous heatmap regression methods. To unify the quantization error induced by different integer operations, we first introduce a unified integer quantization operation as follows. Given a downsampling stride  $s > 1$  and a threshold  $t \in [0, 1]$ , the coordinate  $x \in \mathbb{N}$  then can be quantized according to its fractional part  $\epsilon = x/s - \lfloor x/s \rfloor$ , i.e.,

$$q(x, s, t) = \begin{cases} \lfloor x/s \rfloor & \text{if } \epsilon < t, \\ \lfloor x/s \rfloor + 1 & \text{otherwise.} \end{cases} \quad (10)$$

That is, for integer quantization operations **floor**, **round**, and **ceil**, we have  $t = 1.0$ ,  $t = 0.5$ , and  $t = 0$ , respectively. Furthermore, when the downsampling stride  $s > 1$ , the decode operation in (2) then becomes

$$\mathbf{x}_i^p \in s * \left( \arg \max_{\mathbf{x}} \{\mathbf{h}_i^p(\mathbf{x})\} \right). \quad (11)$$

A vanilla quantization system for heatmap regression can then be formed by the encode operation in (10) and the decode operation in (11). When applied to a vector or a matrix, the integer quantization operation defined in (10) is an element-wise operation.

### 4.3 Quantization Error

In this subsection, we first correct the bias in a vanilla quantization system to form an unbiased vanilla quantization system. With the unbiased quantization system, we then provide a tight upper bound on the quantization error for vanilla heatmap regression.

Let  $\epsilon_x$  denote the fractional part of  $x_i^g/s$ , and  $\epsilon_y$  denote the fractional part of  $y_i^g/s$ . Given the downsampling stride of the heatmap  $s > 1$ , we then have

$$\begin{aligned} \epsilon_x &= x_i^g/s - \lfloor x_i^g/s \rfloor, \\ \epsilon_y &= y_i^g/s - \lfloor y_i^g/s \rfloor. \end{aligned} \quad (12)$$

Given the assumption of a ‘‘perfect’’ heatmap prediction model or no heatmap error, i.e.,  $\mathbf{h}_i^p(\mathbf{x}) = \mathbf{h}_i^g(\mathbf{x})$ , we then have the predicted numerical coordinates

$$\begin{aligned} x_i^p/s &= \begin{cases} \lfloor x_i^g/s \rfloor & \text{if } \epsilon_x < t, \\ \lfloor x_i^g/s \rfloor + 1 & \text{otherwise,} \end{cases} \\ y_i^p/s &= \begin{cases} \lfloor y_i^g/s \rfloor & \text{if } \epsilon_y < t, \\ \lfloor y_i^g/s \rfloor + 1 & \text{otherwise.} \end{cases} \end{aligned}$$

If data samples satisfy the i.i.d. assumption and the fractional parts  $\epsilon_x, \epsilon_y \in \mathbb{U}(0, 1)$ , the bias of  $\mathbf{x}_i^p$  as an estimator of  $\mathbf{x}_i^g$  can then be evaluated as

$$\begin{aligned} \mathbb{E}(x_i^p/s - x_i^g/s) &= \mathbb{E}(\mathbf{1}\{\epsilon_x < t\}(-\epsilon_x) + \mathbf{1}\{\epsilon_x \geq t\}(1 - \epsilon_x)) \\ &= 0.5 - t. \end{aligned}$$

Considering that  $x_i^g, y_i^g$  are independent variables, we thus have the quantization bias in the vanilla quantization system as follows:

$$\begin{aligned} \mathbb{E}(\mathbf{x}_i^p/s - \mathbf{x}_i^g/s) &= (\mathbb{E}(x_i^p/s - x_i^g/s), \mathbb{E}(y_i^p/s - y_i^g/s)) \\ &= (0.5 - t, 0.5 - t). \end{aligned}$$

The quantization biases of the vanilla quantization system with typical integer quantization operations **floor**, **round**, and **ceil** are shown in Table 1. Specifically, when  $t = 0.5$ , the encode operation in (10), i.e., the **round** operation, is unbiased. Furthermore, given  $\forall t \in [0, 1]$  for the encode operation in (10), we can correct the bias of the encode operation with a shift on the decode operation, i.e.,

$$\mathbf{x}_i^p \in s * \left( \arg \max_{\mathbf{x}} \{\mathbf{h}_i^p(\mathbf{x})\} + t - 0.5 \right). \quad (13)$$

TABLE 1

Quantization bias in a vanilla quantization system using typical integer quantization operations, **floor**, **round**, or **ceil**.

Quantization System		Quantization Bias
Encode Operation	Decode Operation	
<b>floor</b>	<b>argmax</b> in (11)	$-s/2$
<b>round</b>	<b>argmax</b> in (11)	0
<b>ceil</b>	<b>argmax</b> in (11)	$s/2$

For simplicity, we always use the **round** operation, i.e.,  $t = 0.5$ , to form an unbiased quantization system as our baseline method. Though the vanilla quantization system defined by (10) and (13) is unbiased, it causes non-invertible localization error. An intuitive explanation for this is that the encode operation directly discards the fractional part of the ground truth numerical coordinates, thus making it impossible for the decode operation to accurately reconstruct the numerical coordinates.

**Theorem 1.** *Given an unbiased quantization system defined by the encode operation in (10) and the decode operation in (13), we then have that the quantization error tightly upper bounded, i.e.,*

$$\|\mathbf{x}_i^p - \mathbf{x}_i^g\|_2 \leq \sqrt{2}s/2,$$

where  $s > 1$  indicates the downsampling stride of the heatmap.

*Proof.* In Appendix. □

From Theorem 1, we know that the vanilla quantization system defined by (10) and (13) will cause non-invertible quantization error and that the upper bound of the quantization error linearly depends on the downsampling stride of the heatmap. As a result, given the heatmap regression model, it will cause extremely large localization error for large faces in the original input image, making it a significant problem in many recent face-related applications such as face makeup, face swapping, and face reenactment.

### 4.4 Randomized Rounding

In vanilla heatmap regression, each numerical coordinate corresponds to a **single activation point** in the heatmap, while the indices of the activation point are all integers. As a result, the fractional part of the numerical coordinate is usually ignored during the encode process, making it an inherent drawback of heatmap regression for sub-pixel localization. To retain the fractional information when using heatmap representations, we utilize multiple activation points around the ground truth activation point. Inspired by the randomized rounding method [27], we address the quantization error in vanilla heatmap regression by using a probabilistic approach. Specifically, we encode the fractional part of the numerical coordinate to different activation points with different activation probabilities. An intuitive example is shown in Fig. 4.

We describe the proposed quantization system as follows. Given the ground truth numerical coordinate  $\mathbf{x}_i^g = (x_i^g, y_i^g)$  and a downsampling stride of the heatmap  $s > 1$ , the ground truth activation point in the heatmap is  $(x_i^g/s, y_i^g/s)$ , which are usually floating-point numbers, and we are unable to find the corresponding pixel in the heatmap. If we ignore the fractional part  $(\epsilon_x, \epsilon_y)$  using a typical integer quantization operation, e.g., **round**, the ground truth activation point will be approximated by one of the activation points around the ground truth activation point, i.e.,  $(\lfloor x_i^g/s \rfloor, \lfloor y_i^g/s \rfloor)$ ,  $(\lfloor x_i^g/s \rfloor + 1, \lfloor y_i^g/s \rfloor)$ ,  $(\lfloor x_i^g/s \rfloor, \lfloor y_i^g/s \rfloor + 1)$ , and  $(\lfloor x_i^g/s \rfloor + 1, \lfloor y_i^g/s \rfloor + 1)$ . However, the above process is not invertible. To address this, we randomly assign the ground-truth activation point to one of the **alternative activation points** around the ground truth

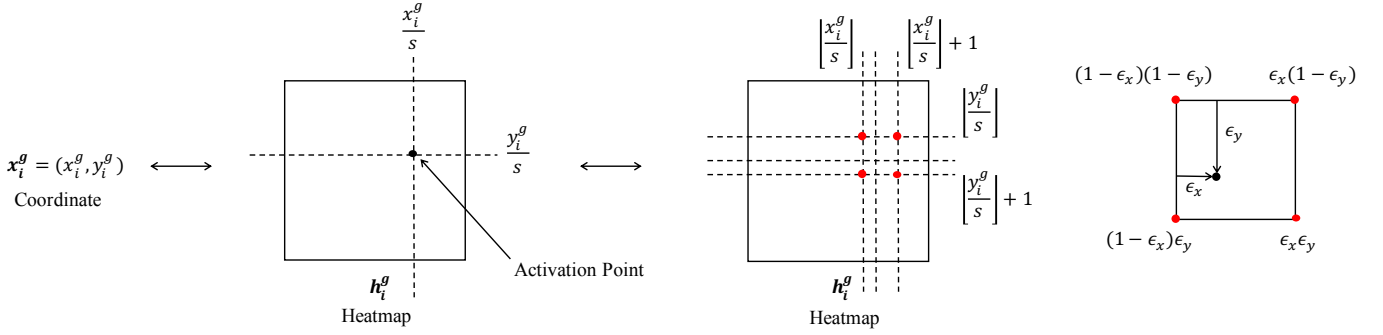


Fig. 4. An intuitive example of the encode operation via randomized rounding. When the downsampling stride  $s > 1$ , the ground truth activation point  $(x_i^g/s, y_i^g/s)$  usually does not correspond to a single pixel in the heatmap. Therefore, we introduce the randomized rounding operation to assign the ground truth activation point to a set of alternative activation points and the activation probability depends on the fractional part of the ground truth numerical coordinates.

activation point, and the activation probability is determined by the fractional part of the ground truth activation point as follows:

$$\begin{aligned}
 P\{\mathbf{h}_i^g(\lfloor x_i^g/s \rfloor, \lfloor y_i^g/s \rfloor) = 1\} &= (1 - \epsilon_x)(1 - \epsilon_y), \\
 P\{\mathbf{h}_i^g(\lfloor x_i^g/s \rfloor + 1, \lfloor y_i^g/s \rfloor) = 1\} &= \epsilon_x(1 - \epsilon_y), \\
 P\{\mathbf{h}_i^g(\lfloor x_i^g/s \rfloor, \lfloor y_i^g/s \rfloor + 1) = 1\} &= (1 - \epsilon_x)\epsilon_y, \\
 P\{\mathbf{h}_i^g(\lfloor x_i^g/s \rfloor + 1, \lfloor y_i^g/s \rfloor + 1) = 1\} &= \epsilon_x\epsilon_y.
 \end{aligned} \tag{14}$$

To achieve the encode scheme in (14) in conjunction with current minibatch stochastic gradient descent training algorithms for deep learning models, we introduce a new integer quantization operation via randomized rounding, i.e., **random-round**:

$$\mathbf{q}(x, s) = \begin{cases} \lfloor x/s \rfloor & \text{if } \epsilon < t, t \sim \mathbb{U}(0, 1), \\ \lfloor x/s \rfloor + 1 & \text{otherwise.} \end{cases} \tag{15}$$

Given the encode operation in (15), if we do not consider the heatmap error, we then have the activation probability at  $\mathbf{x}$ :

$$\mathbf{h}_i^p(\mathbf{x}) = P\{\mathbf{h}_i^g(\mathbf{x}) = 1\}. \tag{16}$$

As a result, the fractional part of the ground truth numerical coordinate  $(\epsilon_x, \epsilon_y)$  can be reconstructed from the predicted heatmap via the activation probabilities of all activation points, i.e.,

$$\mathbf{x}_i^p = s * \left( \sum_{\mathbf{x} \in \mathcal{X}_i^g} \mathbf{h}_i^p(\mathbf{x}) * \mathbf{x} \right), \tag{17}$$

where  $\mathcal{X}_i^g$  indicates the set of activation points around the ground truth activation point, i.e.,

$$\begin{aligned}
 \mathcal{X}_i^g = \{ & (\lfloor x_i^g/s \rfloor, \lfloor y_i^g/s \rfloor), (\lfloor x_i^g/s \rfloor + 1, \lfloor y_i^g/s \rfloor), \\ & (\lfloor x_i^g/s \rfloor, \lfloor y_i^g/s \rfloor + 1), (\lfloor x_i^g/s \rfloor + 1, \lfloor y_i^g/s \rfloor + 1)\}. \end{aligned} \tag{18}$$

**Theorem 2.** *Given the encode operation in (15) and the decode operation in (17), we then have that the 1) encode operation is unbiased; and 2) quantization system is lossless, i.e., there is no quantization error.*

*Proof.* In Appendix.  $\square$

From Theorem 2, we know that the quantization system defined by the encode operation in (15) and the decode operation in (17) is unbiased and lossless.

#### 4.5 Alternative Activation Points

The fractional information of the numerical coordinate  $(\epsilon_x, \epsilon_y)$  is well-captured by the randomized rounding operation, allowing us to reconstruct the ground truth numerical coordinate  $\mathbf{x}_i^g$  without the quantization error. However, during the inference phase, the ground truth numerical coordinate  $\mathbf{x}_i^g$  is unavailable and heatmap error always exists in practice, making it difficult to identify the proper set of ground truth activation points  $\mathcal{X}_i^g$ . In this section, we describe a way to form a set of alternative activation points in practice.

We introduce two activation point selection methods as follows. The first solution is to estimate all activation points via the points around the maximum activation point. As shown in Fig. 5, given the maximum activation point, we then have four different sets of alternative activation points,  $\mathcal{X}_i^{g1}, \mathcal{X}_i^{g2}, \mathcal{X}_i^{g3}$ , and  $\mathcal{X}_i^{g4}$ . Therefore, given the predicted heatmap in practice, we then take a risk of choosing an incorrect set of alternative activation points. To find a robust set of alternative activation points, we may use all nine activation points around the maximum activation point, i.e.,

$$\mathcal{X}_i^g = \mathcal{X}_i^{g1} \cup \mathcal{X}_i^{g2} \cup \mathcal{X}_i^{g3} \cup \mathcal{X}_i^{g4}. \tag{19}$$

Another solution of alternative activation points  $\mathcal{X}_i^g$  is to generalize the **argmax** operation with the **argtopk** operation, i.e., we decode the predicted heatmap  $\mathbf{h}_i^p$  to obtain the numerical coordinate  $\mathbf{x}_i^p$  according to the top  $k$  largest activation points,

$$\mathcal{X}_i^g = \underset{\mathbf{x}}{\text{argtopk}}(\mathbf{h}_i^p(\mathbf{x})). \tag{20}$$

If there is no heatmap error, the two alternative activation points solutions presented above, i.e., the alternative activation points in (18) and (19), are equal to each other when using the decode operation in (17). Specifically, we find that the activation points in (19) achieve comparable performance to the activation points in (20) when  $k = 9$ . For simplicity, unless otherwise mentioned, we use the



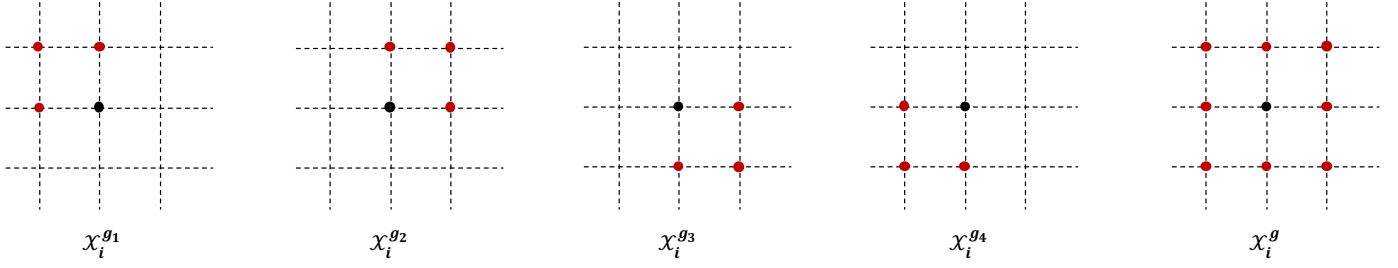


Fig. 5. An example of different possible sets of alternative activation points.

set of alternative activation points defined by (20) in this paper. Furthermore, when we take the heatmap error into consideration, the values of different  $k$  then forms a trade-off on the selection of activation points, i.e., a larger  $k$  will be robust to activation point selection whilst also increasing the risk of noise from the heatmap error. See more discussion in Section 4.6 and the experimental results in Section 5.5.

#### 4.6 Discussion

In this subsection, we provide some insights into the proposed quantization system with respect to: 1) the influence of human annotators and its relationship to the proposed quantization system; and 2) the underlying explanation behind the widely used empirical compensation method “shift a quarter to the second maximum activation point”.

**Unbiased Annotation.** The problem of sub-pixel localization is introduced in Section 4.1, and we assume the “ground truth numerical coordinates” are always accurate. However, the ground truth numerical coordinates are usually labelled by human annotators at the risk of the annotation bias. Given an input image, the ground truth numerical coordinates  $x_i^g$  can be obtained by clicking a specific pixel in the image, which is a simple but effective annotation pipeline provided by most image annotation tools. For sub-pixel numerical coordinates, especially in low-resolution input images, the annotators may click either one of all possible pixels around the ground truth numerical coordinates due to human visual uncertainty. As shown in Fig. 6, clicking any one of the four possible pixels causes annotation error, which corresponds to the fractional part of the ground truth numerical coordinate  $(\epsilon'_x, \epsilon'_y)$ ,

$$(\epsilon'_x, \epsilon'_y) = (x_i^g - \lfloor x_i^g \rfloor, y_i^g - \lfloor y_i^g \rfloor). \quad (21)$$

Given enough data samples, if the annotators click the pixel according to the following distribution, i.e.,

$$\begin{aligned} P\{(\lfloor x_i^g \rfloor, \lfloor y_i^g \rfloor)\} &= (1 - \epsilon'_x)(1 - \epsilon'_y), \\ P\{(\lfloor x_i^g \rfloor + 1, \lfloor y_i^g \rfloor)\} &= \epsilon'_x(1 - \epsilon'_y), \\ P\{(\lfloor x_i^g \rfloor, \lfloor y_i^g \rfloor + 1)\} &= (1 - \epsilon'_x)\epsilon'_y, \\ P\{(\lfloor x_i^g \rfloor + 1, \lfloor y_i^g \rfloor + 1)\} &= \epsilon'_x\epsilon'_y, \end{aligned} \quad (22)$$

the fractional part then can be well captured by the heatmap regression model and we refer to it as an unbiased annotation. Intuitively, we find that an unbiased annotator works in a similar way to the randomized rounding operation, suggesting that we are able to reconstruct the fractional part with the decode operation in (17).

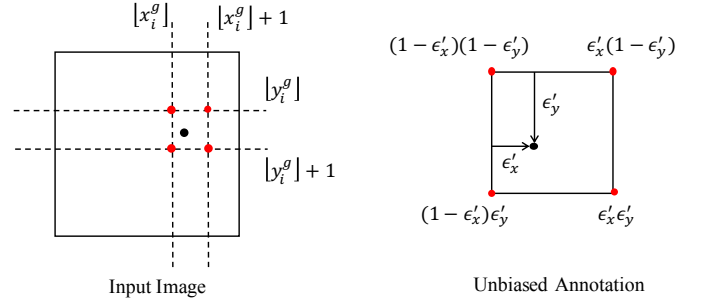


Fig. 6. An example of unbiased human annotation for semantic landmark localization.

If we take the downsampling stride into consideration, the fractional part  $(\epsilon_x, \epsilon_y)$  is then a joint result of both the downsampling of the heatmap and the annotation process, i.e.,

$$(\epsilon_x, \epsilon_y) \propto (\epsilon'_x/s, \epsilon'_y/s) + (s - 1). \quad (23)$$

On the one hand, if the heatmap regression model uses a low input resolution (or a large downsampling stride  $s \gg 1$ ), the fractional part  $(\epsilon_x, \epsilon_y)$  then mainly comes from the downsampling of the heatmap; on the other hand, if the heatmap regression model uses a high input resolution, the annotation process will also have a significant influence on the heatmap regression in practice. When using a low input resolution, the proposed randomized rounding operation captures the fractional part  $(\epsilon_x, \epsilon_y)$  appropriately, and the annotation bias can be ignored; and when using a using a high input resolution, the reconstruction of the fractional part  $(\epsilon_x, \epsilon_y)$  mainly relies on the unbiased annotation process. We demonstrate the distribution of the size of input images via the inter-ocular distance in Fig. 7 and the experimental results in Section 5.5.

**Empirical Compensation.** “Shift a quarter to the second maximum activation point” has become an effective and widely used empirical compensation method for heatmap regression [6], [49], [22], but it still lacks a proper explanation. We therefore provide an intuitive explanation according to the proposed quantization system. The proposed quantization system encodes the ground truth numerical coordinates into multiple activation points, and the activation probability of each activation point is decided by the fractional part, i.e., the activation probability indicates the distance between the activation point and the ground

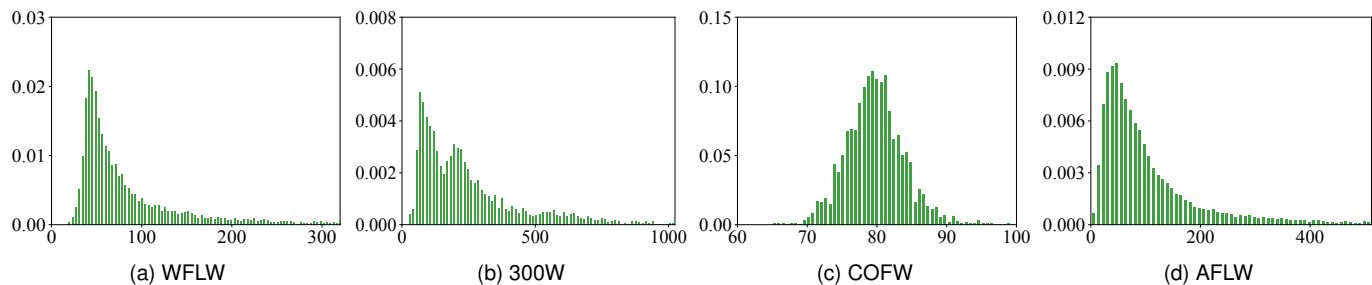


Fig. 7. The histogram of the inter-ocular distance on WFLW, 300W, COFW, and AFLW.

truth activation point. Therefore, the ground-truth activation point is closer to the  $i$ -th maximum activation point than the  $(i + 1)$ -th maximum activation point. We demonstrate the averaged activation probabilities for the top  $k$  activation points on the WFLW dataset in Table 2. We find that the marginal improvement decreases as the number of activation points increases, i.e., the second maximum activation points provides the maximum improvement to the reconstruction of the fractional part. This observation partially explains the effectiveness of the compensation method “shift a quarter to the second maximum activation point”, which can be seen as a special case of the proposed method (20) with  $k = 2$ .

TABLE 2

An evaluation on WFLW to indicate the averaged activation probabilities from the top  $k$  alternative activation points. To demonstrate the effectiveness of different alternative activation points, here we use the heatmap regression model with an input resolution of  $64 \times 64$  pixels.

	k=1	k=2	k=3	k=4
$\bar{h}_i^p(\mathbf{x})$	0.44	0.26	0.17	0.13
NME(%)	6.45	5.07	4.71	4.68

## 5 EXPERIMENTS

In this section, we perform facial landmark detection experiments using heatmap regression. We first introduce widely used datasets for facial landmark detection. We then describe the implementation details of our proposed method. Finally, we present our experimental results on different datasets and perform comprehensive ablation studies on one of the most challenging datasets.

### 5.1 Datasets

We perform semantic landmark localization via heatmap regression on four widely-used facial landmark detection datasets:

- **WFLW** [58]. WFLW contains 10,000 face images, including 7,500 training images and 2,500 testing images, with 98 manually annotated facial landmarks. All face images are selected from the WIDER Face dataset [67], which contains face images with large variations in scale, expression, pose, and occlusion. This is currently the most challenging dataset for facial landmark detection.

- **300W** [68]. 300W contains 3,148 training images, including 337 images from AFW [30], 2,000 images from the training set of HELEN [69], and 811 images from the training set of LFPW [37]. For testing, there are four different settings: 1) **common**: 554 images, including 330 and 224 images from the testsets of HELEN and LFPW, respectively; 2) **challenge**: 135 images from IBUG<sup>1</sup>; 3) **full**: 689 images as a combination of **common** and **challenge**; and 4) **private**: 600 images, including 300 indoor and 300 outdoor images. All images are manually annotated with 68 facial landmarks.
- **COFW** [34]. COFW contains 1,852 images, including 1,345 images for training and 507 images for testing. All images are manually annotated with 29 facial landmarks.
- **AFLW** [70]. AFLW contains 24,386 face images, including 20,000 images for training and 4,386 images for testing. For testing, there are two settings: 1) **full**: all 4,386 images for testing; and 2) **front**: 1,314 frontal images selected from the **full** set. All images are manually annotated with 21 facial landmarks. For fair comparison, we use 19 facial landmarks, i.e., the landmarks on two ears are ignored.

### 5.2 Evaluation Metrics

We use the normalized mean error (NME) as the evaluation metric in this paper, i.e.,

$$\text{NME} = \mathbb{E} \left( \frac{\|\mathbf{x}_i^p - \mathbf{x}_i^g\|_2}{d} \right), \quad (24)$$

where  $d$  indicates the normalization distance. For fair comparison, we report the performances on WFLW, 300W, and COFW using two the normalization methods, **inter-pupil distance** (the distance between the eye centers) and **inter-ocular distance** (the distance between the outer eye corners). We report the performance on AFLW using the size of the face bounding box as the normalization distance, i.e., the normalization distance can be evaluated by  $d = \sqrt{w * h}$ , where  $w$  and  $h$  indicate the width and height of the face bounding box, respectively.

### 5.3 Implementation Details

We implement the proposed heatmap regression method for facial landmark detection using PyTorch [71]. Following the

1. <https://ibug.doc.ic.ac.uk/resources/300-W/>



TABLE 3  
Comparison with State-of-the-Arts on WFLW dataset.

Method	NME (%), Inter-ocular						
	test	pose	expression	illumination	make-up	occlusion	blur
ESR [29]	11.13	25.88	11.47	10.49	11.05	13.75	12.20
SDM [31]	10.29	24.10	11.45	9.32	9.38	13.03	11.28
CFSS [36]	9.07	21.36	10.09	8.30	8.74	11.76	9.96
DVLN [57]	6.08	11.54	6.78	5.73	5.98	7.33	6.88
LAB [58]	5.27	10.24	5.51	5.23	5.15	6.79	6.32
Wing [43]	5.11	8.75	5.36	4.93	5.41	6.37	5.81
3DDE [59]	4.68	8.62	5.21	4.65	4.60	5.77	5.41
DeCaFA [60]	4.62	8.11	4.65	4.41	4.63	5.74	5.38
HRNet [23]	4.60	7.86	4.78	4.57	4.26	5.42	5.36
AVS [61]	4.39	8.42	4.68	4.24	4.37	5.60	4.86
AWing [21]	4.21	7.21	4.46	4.23	4.02	4.99	4.82
H3R (ours)	<b>3.81</b>	<b>6.45</b>	<b>4.07</b>	<b>3.70</b>	<b>3.66</b>	<b>4.48</b>	<b>4.30</b>

TABLE 4  
Comparison with State-of-the-Arts on 300W dataset.

Method	NME (%), Inter-ocular				NME (%), Inter-pupil			
	private	full	common	challenge	private	full	common	challenge
SAN [62]	-	3.98	3.34	6.60	-	-	-	-
DAN [63]	4.30	3.59	3.19	5.24	-	5.03	4.42	7.57
SHN [64]	4.05	-	-	-	-	4.68	4.12	7.00
LAB [58]	-	3.49	2.98	5.19	-	4.12	3.42	6.98
Wing [43]	-	-	-	-	-	<b>4.04</b>	<b>3.27</b>	7.18
DeCaFA [60]	-	3.39	2.93	5.26	-	-	-	-
DFCE [65]	3.88	3.24	2.76	5.22	-	4.55	3.83	7.54
AVS [61]	-	3.86	3.21	6.49	-	4.54	3.98	7.21
HRNet [23]	3.85	3.32	2.87	5.15	-	-	-	-
HG-HSLE [66]	-	3.28	2.85	5.03	-	4.59	3.94	7.24
3DDE [59]	3.73	3.13	2.69	4.92	-	4.39	3.73	7.10
AWing [21]	3.56	3.07	2.72	<b>4.52</b>	-	4.31	3.77	<b>6.52</b>
H3R (ours)	<b>3.48</b>	<b>3.02</b>	<b>2.65</b>	4.58	<b>5.07</b>	4.24	3.67	6.60

practice in [23], we use HRNet [22] as our backbone network, which is an efficient counterpart of ResNet [72] and Hourglass [6] for semantic landmark localization. Unless otherwise mentioned, we use HRNet-W18 as the backbone network in our experiments. All face images are cropped and resized to  $256 \times 256$  pixels and the downsampling stride of the feature map is 4 pixels. For training, we perform widely-used data augmentation for facial landmark detection as follows<sup>2</sup>. We horizontally flip all training images with probability 0.5 and randomly change the brightness ( $\pm 0.125$ ), contrast ( $\pm 0.5$ ), and saturation ( $\pm 0.5$ ) of each image. We then randomly rotate the image ( $\pm 30^\circ$ ), rescale the image ( $\pm 0.25$ ), and translate the image ( $\pm 16$  pixels). We also randomly erase a rectangular region in the training image [73]. All our models are initialized from the weights pretrained on ImageNet [74]. We use the Adam optimizer [75] with batch size 16. The learning rate starts from 0.001 and is divided by 10 for every 60 epochs, with 150 training epochs in total. During the testing phase, we horizontally flip testing images as the data augmentation and average the predictions.

<sup>2</sup> All data augmentation methods used in this paper can be easily implemented by using the common image transformations provided in PyTorch.

## 5.4 Comparison with Current State-of-the-Art

To demonstrate the effectiveness of the proposed method, we compare it with recent state-of-the-art facial landmark detection methods as follows. As shown in Table 3, the proposed method outperforms recent state-of-the-art methods on the most challenging dataset, WFLW, with a clear margin for all different settings. For the 300W dataset, we try to report the performances under different settings for fair comparison. As shown in Table 4, the proposed method achieves comparable performances for all different settings. Specifically, LAB [58] uses the boundary information as the auxiliary supervision; compared to Wing [43], which uses the coordinate regression for semantic landmark localization, the heatmap-based methods usually achieve better performance on the challenge subset. In Table 5, we see that the proposed method outperforms recent state-of-the-art methods with a clear margin on COFW dataset. AFLW captures a wide range of different face poses, including both frontal faces and non-frontal faces. As shown in Table 6, the proposed method achieves consistent improvements for both frontal faces and non-frontal faces, suggesting robustness across different face poses.

## 5.5 Ablation Studies

This paper does not focus on achieving state-of-the-art performance, rather using a simple yet effective baseline to

TABLE 5  
Comparison with State-of-the-Arts on COFW dataset.

Method	NME (%)	
	Inter-ocular	Inter-pupil
SHN [64]	-	5.60
LAB [58]	-	5.58
DFCE [65]	-	5.27
3DDE [59]	-	5.11
Wing [43]	-	5.07
HRNet [23]	3.45	-
AWing [21]	-	4.94
H3R (ours)	<b>3.15</b>	<b>4.55</b>

TABLE 6  
Comparison with State-of-the-Arts on AFLW dataset.

Method	NME (%)	
	full	front
DFCE [65]	2.12	-
3DDE [59]	2.01	-
SAN [62]	1.91	1.85
LAB [58]	1.85	1.62
Wing [43]	1.65	-
HRNet [23]	1.57	1.46
H3R (ours)	<b>1.27</b>	<b>1.11</b>

demonstrate the effectiveness of the proposed quantization system. To better understand the proposed quantization system under different settings, we perform ablation studies on one of the most challenging facial landmark localization datasets, WFLW [58].

**The influence of different input resolutions.** Heatmap regression models use a fixed input resolution, e.g.,  $256 \times 256$  pixels, but training and testing images usually represent a wide range of resolutions. In Fig. 7, we demonstrate the inter-ocular distances of faces in the WFLW dataset, and most faces have an inter-ocular distance of between 30 and 120 pixels. Therefore, we compare the proposed method with the baseline using an input resolution from  $64 \times 64$  pixels to  $512 \times 512$  pixels, i.e., a heatmap resolution from  $16 \times 16$  pixels to  $128 \times 128$  pixels. In Fig. 8, the proposed method significantly improves heatmap regression performance when using a low input resolution. The increasing number of high-resolution images/videos in real-world applications is a challenge with respect to the computational cost and device memory needed to overcome the problem of sub-pixel localization by increasing the input resolution of deep learning-based heatmap regression models. For example, in the film industry, it has sometimes become necessary to swap the appearance of a target actor and a source actor to generate higher fidelity video frames in visual effects, especially when an actor is unavailable for some scenes [76]. The manipulation of actor faces in video frames relies on accurate localization of different facial landmarks and is performed at megapixel resolution, inducing a huge computational cost for extensive frame-by-frame animation. Therefore, instead of using high-resolution input images, our proposed method delivers another efficient solution for dealing with highly accurate semantic landmark

localization.

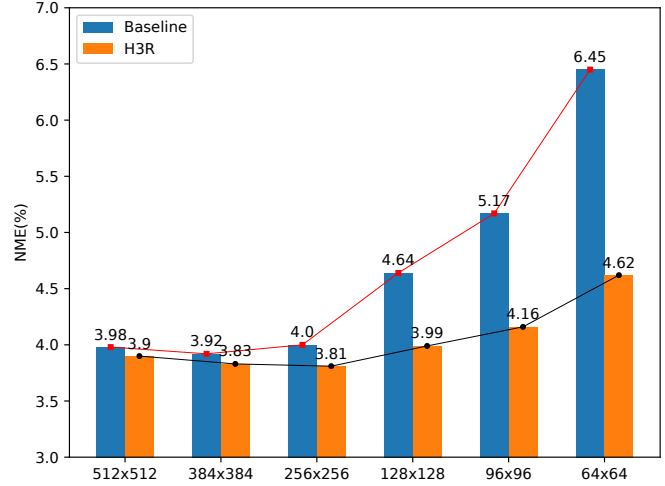


Fig. 8. The influence of different input resolutions. All models use the same backbone network, HRNet-W18, the same number of alternative activation points,  $k = 9$ .

**The influence of different numbers of training samples.** The proposed quantization system does not rely on any assumption about the number of training samples, and is lossless for heatmap regression if there is no heatmap error. However, heatmap prediction performance will be influenced by the number of training samples: increasing the number of training samples improves the model generalizability from learning theory perspective. Therefore, we perform a number of experiments to demonstrate the influence of the proposed method given different numbers of training samples, as shown in Table 7. Specifically, we find that 1) the proposed method delivers consistent improvements when using different numbers of training samples; and 2) increasing the number of training samples improves the performance of the proposed method, especially for heatmap regression models using low-resolution input images.

TABLE 7  
The influence of different numbers of training samples when using different input resolutions. In each cell, the first number indicates the performance of baseline method and the second number indicates the performance of the proposed method.

#Samples	NME (%)		
	$256 \times 256$	$128 \times 128$	$64 \times 64$
256	5.67/5.46	6.02/5.47	7.74/6.20
1024	4.79/4.63	5.27/4.77	7.13/5.43
4096	4.14/3.97	4.81/4.17	6.57/4.76
7500	4.00/3.81	4.62/3.99	6.50/4.62

**The influence of different numbers of alternative activation points.** In the proposed quantization system, the activation probability of each activation point indicates its distance to the ground truth activation point  $(x_i^g/s, y_i^g/s)$ . If there is no heatmap error, the alternative activation points defined in (20) then give the same result as the alternative activation points defined in (18). If the heatmap error cannot

TABLE 8

The influence of different numbers of alternative activation points. For the input resolution  $512 \times 512$  pixels, the best performance is achieved with  $k = 25$ , i.e., NME=3.890; For the input resolution  $384 \times 384$  pixels, the best performance is achieved with  $k = 14$ , i.e., NME=3.825.

Resolution	NME (%)												best
	$k = 1$	$k = 2$	$k = 3$	$k = 4$	$k = 5$	$k = 6$	$k = 7$	$k = 8$	$k = 9$	$k = 10$	$k = 11$	$k = 12$	
$512 \times 512$	3.980	3.946	3.930	3.923	3.916	3.912	3.909	3.906	3.903	3.901	3.898	3.897	<b>3.890</b> / $k = 25$
$384 \times 384$	3.932	3.875	3.855	3.850	3.842	3.837	3.833	3.830	3.828	3.827	3.826	3.826	<b>3.825</b> / $k = 14$
$256 \times 256$	4.005	3.881	3.836	3.832	3.819	3.815	3.810	3.808	<b>3.807</b>	3.807	3.807	3.808	<b>3.807</b> / $k = 9$
$128 \times 128$	4.637	4.164	4.029	4.023	3.997	3.991	<b>3.988</b>	3.989	3.991	3.994	3.998	4.002	<b>3.988</b> / $k = 7$
$96 \times 96$	5.168	4.426	4.215	4.210	4.169	4.163	<b>4.159</b>	4.160	4.163	4.168	4.171	4.175	<b>4.159</b> / $k = 7$
$64 \times 64$	6.447	5.070	4.706	4.704	4.637	4.626	4.618	<b>4.616</b>	4.616	4.618	4.619	4.622	<b>4.616</b> / $k = 8$

TABLE 9

The influence of different numbers of alternative activation points when using Gaussian heatmap. We evaluate the optimal number of alternative activation points when using different standard deviation  $\sigma$  to generate the ground truth heatmap. When  $\sigma = 0$ , the ground truth heatmap is similar to binary heatmap. All heatmap regression models use an input resolution  $256 \times 256$  pixels and the MSE criterion.

	NME (%)												best
	$k = 1$	$k = 2$	$k = 3$	$k = 4$	$k = 5$	$k = 6$	$k = 7$	$k = 8$	$k = 9$	$k = 10$	$k = 11$	$k = 12$	
$\sigma = 0.0$	4.235	4.102	4.069	<b>4.065</b>	4.090	4.202	4.427	4.775	5.219	5.719	6.256	6.802	<b>4.065</b> / $k = 4$
$\sigma = 0.5$	4.162	4.045	4.010	4.008	3.991	3.990	<b>3.988</b>	3.992	3.998	4.014	4.047	4.108	<b>3.988</b> / $k = 7$
$\sigma = 1.0$	4.037	3.928	3.898	3.908	3.871	3.877	3.876	3.876	3.871	3.861	<b>3.855</b>	3.857	<b>3.855</b> / $k = 11$
$\sigma = 1.5$	4.032	3.927	3.901	3.918	3.873	3.879	3.885	3.882	3.878	3.864	3.857	3.860	<b>3.855</b> / $k = 18$
$\sigma = 2.0$	4.086	3.983	3.953	3.969	3.923	3.931	3.937	3.931	3.925	3.909	3.902	3.907	<b>3.894</b> / $k = 25$
$\sigma = 2.5$	4.114	4.021	3.991	4.004	3.958	3.966	3.969	3.962	3.955	3.942	3.933	3.938	<b>3.919</b> / $k = 35$

be ignored, as discussed in Section 4.5, there will be a trade-off with the number of alternative activation points: 1) a small  $k$  increases the risk of missing the activation point within the ground truth alternative activation points; 2) a large  $k$  also introduces additional noise from irrelevant activation points, especially for models with large heatmap error. We demonstrate the performance of the proposed method by using different numbers of alternative activation points, as shown in Table 8. Specifically, we see that 1) when using a high input resolution, the best performance is achieved with a relatively large  $k$ ; and 2) the performance is smooth near the optimal number of alternative activation points, making it easy to choose a proper value of  $k$  for validation data.

As introduced in Section 3, binary heatmaps can be seen as a special case of Gaussian heatmaps with standard deviation  $\sigma = 0$ . Considering that Gaussian heatmaps have been widely used in semantic landmark localization applications, we generalize the proposed quantization system to Gaussian heatmaps and demonstrate the influence of different numbers of alternative activation points in Table 9. Specifically, we see that 1) when applying the proposed quantization system to the model with Gaussian heatmaps, it achieves comparable performance to the model using binary heatmaps; and 2) the optimal number of alternative activation points becomes large as the standard deviation  $\sigma$  increases, e.g., the best performance is achieved with  $\sigma = 1.0$ ,  $k = 11$  and  $\sigma = 1.5$ ,  $k = 18$ .

**The influence of different “bounding box” annotation policies.** To perform facial landmark detection, a reference bounding box is required to indicate the position of the facial area. However, there is a performance gap when using different annotation policies to obtain the reference bounding box [21]. Some examples of different “bounding box” annotation policies are shown in Fig. 9, and we describe

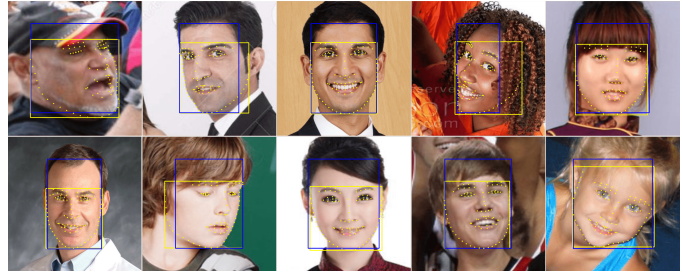


Fig. 9. Two different face “bounding box” annotation policies. **P1**: the yellow face bounding boxes. **P2**: the blue face bounding boxes.

two widely used face bounding box annotation policies for facial landmark localization as follows:

- **P1**: This annotation policy is usually used in semantic landmark localization tasks, especially in facial landmark localization. Specifically, the rectangular area of the bounding box tightly encloses a set of pre-defined facial landmarks.
- **P2**: This annotation policy has been widely used in face detection datasets [67]. The bounding box contains the areas of the forehead, chin, and cheek. For the occluded face, the bounding box is estimated by the human annotator based on the scale of occlusion.

We demonstrate the influence of different annotation policies in Table 10. Specifically, we find that the policy **P1** usually achieves better results, possibly because the occluded forehead (e.g., hair and/or hat) introduces additional variations to the face bounding boxes when using the policy **P2**. Furthermore, in the cross-policy comparison, we find that the heatmap regression model using the policy **P2** is



TABLE 10  
The influence of different face “bounding box” annotation policies.

Policy		NME (%), Inter-ocular						
training	testing	test	pose	expression	illumination	make-up	occlusion	blur
P1	P1	3.81	6.45	4.07	3.70	3.66	4.48	4.30
P2	P2	3.95	6.74	4.17	3.89	3.81	4.73	4.51
P1	P2	5.34	9.68	5.24	5.25	5.57	6.55	6.14
P2	P1	4.04	6.90	4.24	3.99	3.90	4.87	4.65

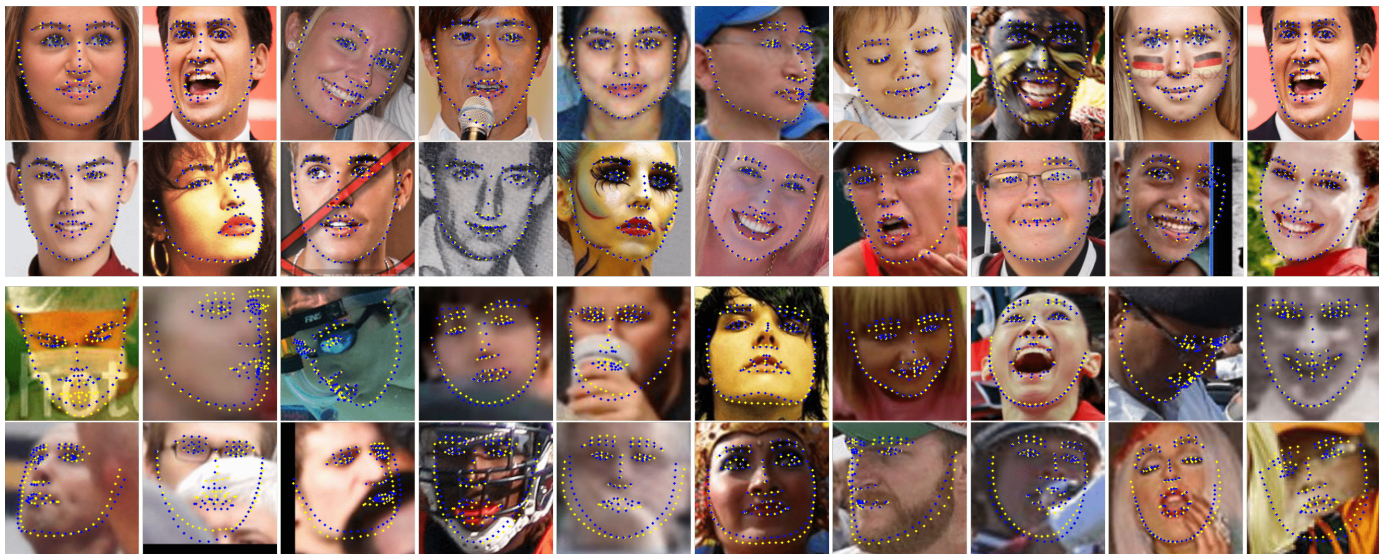


Fig. 10. Qualitative results from the test split of the WFLW dataset (best view in color). **Blue**: the ground truth facial landmarks. **Yellow**: the predicted facial landmarks. The first two rows show some “good” cases and the last two rows show some “bad” cases.

insensitive to “inaccurate” face bounding boxes during testing, suggesting that it will be more robust to the inaccurate bounding boxes provided by the face detection algorithms.

**Qualitative analysis.** In Fig. 10, we present some “good” cases and “bad” examples of facial landmark detection according to the normalized mean error (NME). Specifically, for the good cases presented in the first two rows, most images are of high quality. For the bad cases in the last two rows, most images contain heavy blurring and/or occlusion, making it difficult to accurately identify the contours of different parts of the faces. Among the failure cases, we also find that some predicted facial landmarks seems to be more “accurate” than the “ground truth facial landmarks” labelled by human annotators. That is, some annotation bias exists for different human annotators to label face images with heavy blur or occlusion. Therefore, it is important to find a proper way to deal with uncertainty in facial landmark annotations provided by human annotators, especially for poor-quality images.

## 6 CONCLUSION

In this paper, we address the problem of sub-pixel localization for heatmap-based semantic landmark localization. We formally analyze quantization error in vanilla heatmap regression and propose a new quantization system via randomized rounding, which we prove is unbiased and lossless. Experiments on facial landmark localization datasets

demonstrate the effectiveness of the proposed quantization system for sub-pixel localization. A main limitation of the proposed method is the assumption of unbiased human annotation, especially when using very high input resolutions. The proposed quantization system might be at risk of overfitting the annotation bias introduced by human annotators, which will be the subject of future study.

## REFERENCES

- [1] Y. Sun, X. Wang, and X. Tang, “Deep convolutional network cascade for facial point detection,” in *IEEE Conference on Computer Vision and Pattern Recognition (CVPR)*, 2013, pp. 3476–3483.
- [2] A. Bulat and G. Tzimiropoulos, “How far are we from solving the 2d & 3d face alignment problem?(and a dataset of 230,000 3d facial landmarks),” in *IEEE International Conference on Computer Vision (ICCV)*, 2017, pp. 1021–1030.
- [3] A. Sinha, C. Choi, and K. Ramani, “Deephand: Robust hand pose estimation by completing a matrix imputed with deep features,” in *IEEE Conference on Computer Vision and Pattern Recognition (CVPR)*, June 2016.
- [4] U. Iqbal, P. Molchanov, T. Breuel Juergen Gall, and J. Kautz, “Hand pose estimation via latent 2.5 d heatmap regression,” in *European Conference on Computer Vision (ECCV)*, 2018, pp. 118–134.
- [5] A. Toshev and C. Szegedy, “DeepPose: Human pose estimation via deep neural networks,” in *IEEE Conference on Computer Vision and Pattern Recognition (CVPR)*, 2014, pp. 1653–1660.
- [6] A. Newell, K. Yang, and J. Deng, “Stacked hourglass networks for human pose estimation,” in *European Conference on Computer Vision (ECCV)*. Springer, 2016, pp. 483–499.

- [7] A. Saxena, J. Driemeyer, and A. Y. Ng, "Robotic grasping of novel objects using vision," *International Journal of Robotics Research (IJRR)*, vol. 27, no. 2, pp. 157–173, 2008. [Online]. Available: <https://doi.org/10.1177/0278364907087172>
- [8] Y. Sun, Y. Chen, X. Wang, and X. Tang, "Deep learning face representation by joint identification-verification," in *Neural Information Processing Systems (NIPS)*, 2014, pp. 1988–1996.
- [9] J. Thies, M. Zollhofer, M. Stamminger, C. Theobalt, and M. Nießner, "Face2face: Real-time face capture and reenactment of rgb videos," in *IEEE Conference on Computer Vision and Pattern Recognition (CVPR)*, 2016, pp. 2387–2395.
- [10] C. Wang, D. Xu, Y. Zhu, R. Martín-Martín, C. Lu, L. Fei-Fei, and S. Savarese, "Densefusion: 6d object pose estimation by iterative dense fusion," in *IEEE Conference on Computer Vision and Pattern Recognition (CVPR)*, 2019.
- [11] J. Deng, J. Guo, X. Niannan, and S. Zafeiriou, "Arcface: Additive angular margin loss for deep face recognition," in *IEEE Conference on Computer Vision and Pattern Recognition (CVPR)*, 2019.
- [12] H. Zhao, M. Tian, S. Sun, J. Shao, J. Yan, S. Yi, X. Wang, and X. Tang, "Spindle net: Person re-identification with human body region guided feature decomposition and fusion," in *IEEE Conference on Computer Vision and Pattern Recognition (CVPR)*, 2017, pp. 1077–1085.
- [13] L. Zheng, Y. Huang, H. Lu, and Y. Yang, "Pose-invariant embedding for deep person re-identification," *IEEE Transactions on Image Processing (TIP)*, vol. 28, no. 9, pp. 4500–4509, 2019.
- [14] Y.-C. Chen, X. Shen, and J. Jia, "Makeup-go: Blind reversion of portrait edit," in *IEEE International Conference on Computer Vision (ICCV)*, Oct 2017.
- [15] H. Chang, J. Lu, F. Yu, and A. Finkelstein, "Pairedcyclegan: Asymmetric style transfer for applying and removing makeup," in *IEEE Conference on Computer Vision and Pattern Recognition (CVPR)*, 2018, pp. 40–48.
- [16] C. Cao, Y. Weng, S. Lin, and K. Zhou, "3d shape regression for real-time facial animation," *ACM Transactions on Graphics (TOG)*, vol. 32, no. 4, pp. 1–10, 2013.
- [17] C. Cao, Q. Hou, and K. Zhou, "Displaced dynamic expression regression for real-time facial tracking and animation," *ACM Transactions on Graphics (TOG)*, vol. 33, no. 4, pp. 1–10, 2014.
- [18] J. Thies, M. Zollhofer, M. Nießner, L. Valgaerts, M. Stamminger, and C. Theobalt, "Real-time expression transfer for facial reenactment," *ACM Transactions on Graphics (TOG)*, vol. 34, no. 6, pp. 183–1, 2015.
- [19] J. J. Tompson, A. Jain, Y. LeCun, and C. Bregler, "Joint training of a convolutional network and a graphical model for human pose estimation," in *Neural Information Processing Systems (NIPS)*, 2014, pp. 1799–1807.
- [20] A. Nibali, Z. He, S. Morgan, and L. Prendergast, "Numerical coordinate regression with convolutional neural networks," *arXiv preprint arXiv:1801.07372*, 2018.
- [21] X. Wang, L. Bo, and L. Fuxin, "Adaptive wing loss for robust face alignment via heatmap regression," in *IEEE International Conference on Computer Vision (ICCV)*, 2019, pp. 6971–6981.
- [22] K. Sun, B. Xiao, D. Liu, and J. Wang, "Deep high-resolution representation learning for human pose estimation," in *IEEE Conference on Computer Vision and Pattern Recognition (CVPR)*, 2019, pp. 5693–5703.
- [23] J. Wang, K. Sun, T. Cheng, B. Jiang, C. Deng, Y. Zhao, D. Liu, Y. Mu, M. Tan, X. Wang, W. Liu, and B. Xiao, "Deep high-resolution representation learning for visual recognition," *IEEE Transactions on Pattern Analysis and Machine Intelligence (TPAMI)*, 2020.
- [24] Y. Tai, Y. Liang, X. Liu, L. Duan, J. Li, C. Wang, F. Huang, and Y. Chen, "Towards highly accurate and stable face alignment for high-resolution videos," in *AAAI Conference on Artificial Intelligence (AAAI)*, vol. 33, 2019, pp. 8893–8900.
- [25] W. Li, Z. Wang, B. Yin, Q. Peng, Y. Du, T. Xiao, G. Yu, H. Lu, Y. Wei, and J. Sun, "Rethinking on multi-stage networks for human pose estimation," *arXiv preprint arXiv:1901.00148*, 2019.
- [26] F. Zhang, X. Zhu, H. Dai, M. Ye, and C. Zhu, "Distribution-aware coordinate representation for human pose estimation," in *IEEE Conference on Computer Vision and Pattern Recognition (CVPR)*, 2020, pp. 7093–7102.
- [27] P. Raghavan and C. D. Tompson, "Randomized rounding: a technique for provably good algorithms and algorithmic proofs," *Combinatorica*, vol. 7, no. 4, pp. 365–374, 1987.
- [28] B. Korte, J. Vygen, B. Korte, and J. Vygen, *Combinatorial optimization*. Springer, 2012, vol. 2.
- [29] X. Cao, Y. Wei, F. Wen, and J. Sun, "Face alignment by explicit shape regression," *International Journal of Computer Vision (IJCV)*, vol. 107, no. 2, pp. 177–190, 2014.
- [30] X. Zhu and D. Ramanan, "Face detection, pose estimation, and landmark localization in the wild," in *IEEE Conference on Computer Vision and Pattern Recognition (CVPR)*. IEEE, 2012, pp. 2879–2886.
- [31] X. Xiong and F. De la Torre, "Supervised descent method and its applications to face alignment," in *IEEE Conference on Computer Vision and Pattern Recognition (CVPR)*, 2013, pp. 532–539.
- [32] S. Ren, X. Cao, Y. Wei, and J. Sun, "Face alignment at 3000 fps via regressing local binary features," in *IEEE Conference on Computer Vision and Pattern Recognition (CVPR)*, 2014, pp. 1685–1692.
- [33] V. Kazemi and J. Sullivan, "One millisecond face alignment with an ensemble of regression trees," in *IEEE Conference on Computer Vision and Pattern Recognition (CVPR)*, 2014, pp. 1867–1874.
- [34] X. P. Burgos-Artizzu, P. Perona, and P. Dollár, "Robust face landmark estimation under occlusion," in *IEEE International Conference on Computer Vision (ICCV)*, 2013, pp. 1513–1520.
- [35] J. Zhang, S. Shan, M. Kan, and X. Chen, "Coarse-to-fine auto-encoder networks (cfan) for real-time face alignment," in *European Conference on Computer Vision (ECCV)*. Springer, 2014, pp. 1–16.
- [36] S. Zhu, C. Li, C. Change Loy, and X. Tang, "Face alignment by coarse-to-fine shape searching," in *IEEE Conference on Computer Vision and Pattern Recognition (CVPR)*, 2015, pp. 4998–5006.
- [37] P. N. Belhumeur, D. W. Jacobs, D. J. Kriegman, and N. Kumar, "Localizing parts of faces using a consensus of exemplars," *IEEE Transactions on Pattern Analysis and Machine Intelligence (TPAMI)*, vol. 35, no. 12, pp. 2930–2940, 2013.
- [38] X. Miao, X. Zhen, X. Liu, C. Deng, V. Athitsos, and H. Huang, "Direct shape regression networks for end-to-end face alignment," in *IEEE Conference on Computer Vision and Pattern Recognition (CVPR)*, 2018, pp. 5040–5049.
- [39] Z. Zhang, P. Luo, C. C. Loy, and X. Tang, "Facial landmark detection by deep multi-task learning," in *European Conference on Computer Vision (ECCV)*. Springer, 2014, pp. 94–108.
- [40] K. Zhang, Z. Zhang, Z. Li, and Y. Qiao, "Joint face detection and alignment using multitask cascaded convolutional networks," *IEEE Signal Processing Letters*, vol. 23, no. 10, pp. 1499–1503, 2016.
- [41] R. Ranjan, V. M. Patel, and R. Chellappa, "Hyperface: A deep multi-task learning framework for face detection, landmark localization, pose estimation, and gender recognition," *IEEE Transactions on Pattern Analysis and Machine Intelligence (TPAMI)*, vol. 41, no. 1, pp. 121–135, 2017.
- [42] R. Girshick, "Fast r-cnn," in *IEEE International Conference on Computer Vision (ICCV)*, 2015, pp. 1440–1448.
- [43] Z.-H. Feng, J. Kittler, M. Awais, P. Huber, and X.-J. Wu, "Wing loss for robust facial landmark localisation with convolutional neural networks," in *IEEE Conference on Computer Vision and Pattern Recognition (CVPR)*, 2018, pp. 2235–2245.
- [44] A. Bulat and G. Tzimiropoulos, "Binarized convolutional landmark localizers for human pose estimation and face alignment with limited resources," in *IEEE International Conference on Computer Vision (ICCV)*, 2017, pp. 3706–3714.
- [45] D. Merget, M. Rock, and G. Rigoll, "Robust facial landmark detection via a fully-convolutional local-global context network," in *IEEE Conference on Computer Vision and Pattern Recognition (CVPR)*, 2018, pp. 781–790.
- [46] T. Pfister, J. Charles, and A. Zisserman, "Flowing convnets for human pose estimation in videos," in *IEEE International Conference on Computer Vision (ICCV)*, 2015, pp. 1913–1921.
- [47] S.-E. Wei, V. Ramakrishna, T. Kanade, and Y. Sheikh, "Convolutional pose machines," in *IEEE Conference on Computer Vision and Pattern Recognition (CVPR)*, 2016, pp. 4724–4732.
- [48] Z. Cao, T. Simon, S.-E. Wei, and Y. Sheikh, "Realtime multi-person 2d pose estimation using part affinity fields," in *IEEE Conference on Computer Vision and Pattern Recognition (CVPR)*, 2017, pp. 7291–7299.
- [49] Y. Chen, Z. Wang, Y. Peng, Z. Zhang, G. Yu, and J. Sun, "Cascaded pyramid network for multi-person pose estimation," in *IEEE Conference on Computer Vision and Pattern Recognition (CVPR)*, 2018, pp. 7103–7112.
- [50] G. Papandreou, T. Zhu, N. Kanazawa, A. Toshev, J. Tompson, C. Bregler, and K. Murphy, "Towards accurate multi-person pose estimation in the wild," in *IEEE Conference on Computer Vision and Pattern Recognition (CVPR)*, 2017, pp. 4903–4911.

- [51] X. Sun, B. Xiao, F. Wei, S. Liang, and Y. Wei, "Integral human pose regression," in *European Conference on Computer Vision (ECCV)*, 2018, pp. 529–545.
- [52] D. C. Luvizon, D. Picard, and H. Tabia, "2d/3d pose estimation and action recognition using multitask deep learning," in *IEEE Conference on Computer Vision and Pattern Recognition (CVPR)*, 2018, pp. 5137–5146.
- [53] D. C. Luvizon, H. Tabia, and D. Picard, "Human pose regression by combining indirect part detection and contextual information," *Computers & Graphics*, vol. 85, pp. 15–22, 2019.
- [54] K. M. Yi, E. Trulls, V. Lepetit, and P. Fua, "Lift: Learned invariant feature transform," in *European Conference on Computer Vision (ECCV)*. Springer, 2016, pp. 467–483.
- [55] S. Levine, C. Finn, T. Darrell, and P. Abbeel, "End-to-end training of deep visuomotor policies," *Journal of Machine Learning Research (JMLR)*, vol. 17, no. 1, pp. 1334–1373, 2016.
- [56] J. Thewlis, H. Bilen, and A. Vedaldi, "Unsupervised learning of object landmarks by factorized spatial embeddings," in *IEEE International Conference on Computer Vision (ICCV)*, 2017, pp. 5916–5925.
- [57] W. Wu and S. Yang, "Leveraging intra and inter-dataset variations for robust face alignment," in *IEEE Conference on Computer Vision and Pattern Recognition Workshops (CVPRW)*, 2017, pp. 150–159.
- [58] W. Wu, C. Qian, S. Yang, Q. Wang, Y. Cai, and Q. Zhou, "Look at boundary: A boundary-aware face alignment algorithm," in *IEEE Conference on Computer Vision and Pattern Recognition (CVPR)*, 2018, pp. 2129–2138.
- [59] R. Valle, J. M. Buenaposada, A. Valdés, and L. Baumela, "Face alignment using a 3d deeply-initialized ensemble of regression trees," *Computer Vision and Image Understanding (CVIU)*, vol. 189, p. 102846, 2019.
- [60] A. Dapogny, K. Bailly, and M. Cord, "Decafa: Deep convolutional cascade for face alignment in the wild," in *IEEE International Conference on Computer Vision (ICCV)*, October 2019.
- [61] S. Qian, K. Sun, W. Wu, C. Qian, and J. Jia, "Aggregation via separation: Boosting facial landmark detector with semi-supervised style translation," in *IEEE International Conference on Computer Vision (ICCV)*, 2019, pp. 10 153–10 163.
- [62] X. Dong, Y. Yan, W. Ouyang, and Y. Yang, "Style aggregated network for facial landmark detection," in *IEEE Conference on Computer Vision and Pattern Recognition (CVPR)*, 2018, pp. 379–388.
- [63] M. Kowalski, J. Naruniec, and T. Trzcinski, "Deep alignment network: A convolutional neural network for robust face alignment," in *IEEE Conference on Computer Vision and Pattern Recognition Workshops (CVPRW)*, 2017, pp. 88–97.
- [64] J. Yang, Q. Liu, and K. Zhang, "Stacked hourglass network for robust facial landmark localisation," in *IEEE Conference on Computer Vision and Pattern Recognition Workshops (CVPRW)*, 2017, pp. 79–87.
- [65] R. Valle, J. M. Buenaposada, A. Valdés, and L. Baumela, "A deeply-initialized coarse-to-fine ensemble of regression trees for face alignment," in *European Conference on Computer Vision (ECCV)*, 2018, pp. 585–601.
- [66] X. Zou, S. Zhong, L. Yan, X. Zhao, J. Zhou, and Y. Wu, "Learning robust facial landmark detection via hierarchical structured ensemble," in *IEEE International Conference on Computer Vision (ICCV)*, October 2019.
- [67] S. Yang, P. Luo, C.-C. Loy, and X. Tang, "Wider face: A face detection benchmark," in *IEEE Conference on Computer Vision and Pattern Recognition (CVPR)*, 2016, pp. 5525–5533.
- [68] C. Sagonas, G. Tzimiropoulos, S. Zafeiriou, and M. Pantic, "300 faces in-the-wild challenge: The first facial landmark localization challenge," in *IEEE International Conference on Computer Vision Workshops (ICCVW)*, 2013, pp. 397–403.
- [69] V. Le, J. Brandt, Z. Lin, L. Bourdev, and T. S. Huang, "Interactive facial feature localization," in *European Conference on Computer Vision (ECCV)*. Springer, 2012, pp. 679–692.
- [70] M. Koestinger, P. Wohlhart, P. M. Roth, and H. Bischof, "Annotated facial landmarks in the wild: A large-scale, real-world database for facial landmark localization," in *IEEE International Conference on Computer Vision Workshops (ICCVW)*. IEEE, 2011, pp. 2144–2151.
- [71] A. Paszke, S. Gross, F. Massa, A. Lerer, J. Bradbury, G. Chanan, T. Killeen, Z. Lin, N. Gimeshein, L. Antiga, A. Desmaison, A. Kopf, E. Yang, Z. DeVito, M. Raison, A. Tejani, S. Chilamkurthy, B. Steiner, L. Fang, J. Bai, and S. Chintala, "Pytorch: An imperative style, high-performance deep learning library," in *Neural Information Processing Systems (NIPS)*, H. Wallach, H. Larochelle, A. Beygelzimer, F. d Alché-Buc, E. Fox, and R. Garnett, Eds. Curran Associates, Inc., 2019, pp. 8024–8035.
- [72] K. He, X. Zhang, S. Ren, and J. Sun, "Deep residual learning for image recognition," in *IEEE Conference on Computer Vision and Pattern Recognition (CVPR)*, 2016, pp. 770–778.
- [73] Z. Zhong, L. Zheng, G. Kang, S. Li, and Y. Yang, "Random erasing data augmentation," *AAAI Conference on Artificial Intelligence (AAAI)*, 2020.
- [74] J. Deng, W. Dong, R. Socher, L.-J. Li, K. Li, and L. Fei-Fei, "Imagenet: A large-scale hierarchical image database," in *IEEE Conference on Computer Vision and Pattern Recognition (CVPR)*. Ieee, 2009, pp. 248–255.
- [75] D. P. Kingma and J. Ba, "Adam: A method for stochastic optimization," in *International Conference on Learning Representations (ICLR)*, 2015.
- [76] J. Naruniec, L. Helmingier, C. Schroers, and R. Weber, "High-resolution neural face swapping for visual effects," *Eurographics Symposium on Rendering*, vol. 39, no. 4, 2020.
- [77] M. Andriluka, L. Pishchulin, P. Gehler, and B. Schiele, "2d human pose estimation: New benchmark and state of the art analysis," in *IEEE Conference on Computer Vision and Pattern Recognition (CVPR)*, 2014, pp. 3686–3693.
- [78] T.-Y. Lin, M. Maire, S. Belongie, J. Hays, P. Perona, D. Ramanan, P. Dollár, and C. L. Zitnick, "Microsoft coco: Common objects in context," in *European Conference on Computer Vision (ECCV)*. Springer, 2014, pp. 740–755.



**Baosheng Yu** received a B.E. from the University of Science and Technology of China in 2014, and a Ph.D. from The University of Sydney in 2019. He is currently a Research Fellow in the School of Computer Science and the Faculty of Engineering at The University of Sydney, NSW, Australia. His research interests include machine learning, computer vision, and deep learning.



**Dacheng Tao (F15)** is currently a Professor of Computer Science and an ARC Laureate Fellow in the School of Computer Science and the Faculty of Engineering at The University of Sydney. He mainly applies statistics and mathematics to artificial intelligence and data science. His research is in detailed in one monograph and over 200 publications in prestigious journals and proceedings at prominent conferences such as IEEE T-PAMI, T-IP, NIPS, ICML, CVPR, ICCV, ECCV, AAAI, IJCAI, and ICDM and ACM SIGKDD, with several best paper awards, such as the Best Theory/Algorithm Paper Runner Up Award at the IEEE ICDM07, the Distinguished Paper Award at the 2018 IJCAI, the 2014 ICDM 10-year Highest-Impact Paper Award, and the 2017 IEEE Signal Processing Society Best Paper Award. He received the 2015 Australian Scopus-Eureka Prize and the 2018 IEEE ICDM Research Contributions Award. He is a fellow of the Australian Academy of Science, AAAS, ACM and IEEE.



## APPENDIX A

### PROOFS OF THEOREM 1 AND THEOREM 2

**Theorem 1.** *Given an unbiased quantization system defined by the encode operation in (10) and the decode operation in (13), we then have that the quantization error tightly upper bounded, i.e.,*

$$\|\mathbf{x}_i^p - \mathbf{x}_i^g\|_2 \leq \sqrt{2}s/2,$$

where  $s > 1$  indicates the downsampling stride of the heatmap.

*Proof.* Given the ground truth numerical coordinate  $\mathbf{x}_i^g = (x_i^g, y_i^g)$ , the predicted numerical coordinate  $\mathbf{x}_i^p = (x_i^p, y_i^p)$ , and the downsampling stride of the heatmap  $s > 1$ , if there is no heatmap error, we then have

$$\mathbf{h}_i^p(\mathbf{x}) = \mathbf{h}_i^g(\mathbf{x}),$$

where  $\mathbf{h}_i^p(\mathbf{x})$  and  $\mathbf{h}_i^g(\mathbf{x})$  indicate the ground-truth heatmap and the predicted heatmap, respectively. Therefore, according to the decode operation in (13), we have the predicted numerical coordinate as

$$x_i^p/s = \begin{cases} \lfloor x_i^g/s \rfloor + t - 0.5 & \text{if } \epsilon_x < t, \\ \lfloor x_i^g/s \rfloor + t + 0.5 & \text{otherwise.} \end{cases}$$

$$y_i^p/s = \begin{cases} \lfloor y_i^g/s \rfloor + t - 0.5 & \text{if } \epsilon_y < t, \\ \lfloor y_i^g/s \rfloor + t + 0.5 & \text{otherwise.} \end{cases}$$

where  $\epsilon_x = x_i^g/s - \lfloor x_i^g/s \rfloor$  and  $\epsilon_y = y_i^g/s - \lfloor y_i^g/s \rfloor$ . The quantization error of vanilla quantization system then can be evaluated as follows:

$$|x_i^p/s - x_i^g/s| = \begin{cases} |t - \epsilon_x - 0.5| & \text{if } \epsilon_x < t, \\ |t - \epsilon_x + 0.5| & \text{otherwise.} \end{cases}$$

$$|y_i^p/s - y_i^g/s| = \begin{cases} |t - \epsilon_y - 0.5| & \text{if } \epsilon_y < t, \\ |t - \epsilon_y + 0.5| & \text{otherwise.} \end{cases}$$

The maximum quantization error  $|x_i^p - x_i^g| = s/2$  is achieved when  $\epsilon_x = t$ . Similarly, we have the maximum quantization error  $|y_i^p - y_i^g| = s/2$  is achieved with  $\epsilon_y = t$ . Considering that  $x_i^p$  and  $y_i^p$  are linearly independent variables, we thus have

$$\|\mathbf{x}_i^p - \mathbf{x}_i^g\|_2 = \sqrt{(x_i^p - x_i^g)^2 + (y_i^p - y_i^g)^2} \leq \sqrt{2}s/2.$$

The maximum quantization error is achieved with  $\epsilon_x = \epsilon_y = t$ . That is, the quantization error in vanilla quantization system is tightly upper bounded by  $\sqrt{2}s/2$ .  $\square$

**Theorem 2.** *Given the encode operation in (15) and the decode operation in (17), we then have that the 1) encode operation is unbiased; and 2) quantization system is lossless, i.e., there is no quantization error.*

*Proof.* Given the ground-truth numerical coordinate  $\mathbf{x}_i^g = (x_i^g, y_i^g)$ , the predicted numerical coordinate  $\mathbf{x}_i^p = (x_i^p, y_i^p)$ , and the downsampling stride of the heatmap  $s > 1$ , we then have

$$\begin{aligned} \mathbb{E}(\mathbf{q}(\mathbf{x}_i^g, s)) &= \mathbb{E}(P\{\epsilon_x < t\} \lfloor x_i^g/s \rfloor + P\{\epsilon_x \geq t\} (\lfloor x_i^g/s \rfloor + 1)) \\ &= \lfloor x_i^g/s \rfloor (1 - \epsilon_x) + (\lfloor x_i^g/s \rfloor + 1)\epsilon_x \\ &= x_i^g/s \end{aligned}$$

Similarly, we have  $\mathbb{E}(\mathbf{q}(y_i^g, s)) = y_i^g/s$ . Considering that  $x_i^p$  and  $y_i^p$  are linearly independent variables, we thus have

$$\begin{aligned} \mathbb{E}(\mathbf{q}(\mathbf{x}_i^g, s)) &= (\mathbb{E}(\mathbf{q}(x_i^g, s)), \mathbb{E}(\mathbf{q}(y_i^g, s))) \\ &= (x_i^g/s, y_i^g/s). \end{aligned}$$

Therefore, the encode operation in (15), i.e., **random-round**, is an unbiased encode operation for heatmap regression.

We then prove that the quantization system is losses as follows. For the decode operation in (17), if there is no heatmap error, we then have

$$\begin{aligned} P\{\mathbf{x}_i^p/s = (\lfloor x_i^g/s \rfloor, \lfloor y_i^g/s \rfloor)\} &= (1 - \epsilon_x)(1 - \epsilon_y), \\ P\{\mathbf{x}_i^p/s = (\lfloor x_i^g/s \rfloor + 1, \lfloor y_i^g/s \rfloor)\} &= \epsilon_x(1 - \epsilon_y), \\ P\{\mathbf{x}_i^p/s = (\lfloor x_i^g/s \rfloor, \lfloor y_i^g/s \rfloor + 1)\} &= (1 - \epsilon_x)\epsilon_y, \\ P\{\mathbf{x}_i^p/s = (\lfloor x_i^g/s \rfloor + 1, \lfloor y_i^g/s \rfloor + 1)\} &= \epsilon_x\epsilon_y. \end{aligned}$$

We can reconstruct the fractional part of  $\mathbf{x}_i^g$ , i.e.,

$$\begin{aligned} (x_i^p/s, y_i^p/s) &= \sum_{\mathbf{x}_i^p} P\{\mathbf{x}_i^p\} \mathbf{x}_i^p/s \\ &= (\lfloor x_i^g/s \rfloor, \lfloor y_i^g/s \rfloor) * (1 - \epsilon_x)(1 - \epsilon_y) \\ &\quad + (\lfloor x_i^g/s \rfloor + 1, \lfloor y_i^g/s \rfloor) * \epsilon_x(1 - \epsilon_y) \\ &\quad + (\lfloor x_i^g/s \rfloor, \lfloor y_i^g/s \rfloor + 1) * (1 - \epsilon_x)\epsilon_y \\ &\quad + (\lfloor x_i^g/s \rfloor + 1, \lfloor y_i^g/s \rfloor + 1) * \epsilon_x\epsilon_y \\ &= (x_i^g/s, y_i^g/s). \end{aligned}$$

That is,  $(x_i^p, y_i^p) = (x_i^g, y_i^g)$ , i.e., there is no quantization error.  $\square$

## APPENDIX B

### EXPERIMENTS ON HUMAN POSE ESTIMATION

The proposed quantization system can be easily integrated into most of heatmap regression models. As shown in 5.5, the proposed quantization system can be well generalized to Gaussian heatmap, which has been very popular in deep learning-based human pose estimation. To further demonstrate the effectiveness of the proposed quantization system for semantic landmark localization, we perform experiments on human pose estimation and evaluate the performance on two popular datasets,

- **MPII** [77]: The MPII Human Pose dataset contains around 28,821 images with 40,522 person instances, in which 11,701 images for testing and the remaining 17,120 images for training. Following the experimental setup in [22], we use 22,246 person instances for training and evaluate the performance on the MPII validation set with 2,958 person instances, which is a heldout subset of MPII training set.
- **COCO** [78]: The COCO dataset contains over 200,000 images and 250,000 person instances, in which each person instance is labeled with 17 keypoints. Following the experimental setup in [22], we evaluate the proposed method on the validation set with 5,000 images.

TABLE 11

Results on MPII Human Pose dataset. In each block, the first row indicates the performance of pretrained model by [22] using the compensation method “shift a quarter to the second maximum activation point”; The second row with  $\checkmark$  indicates the performance when using the proposed method only in inference stage; The third row with  $\checkmark\checkmark$  (if exist) indicates the performance when using the proposed method in both training and inference stages.

Backbone	Input	H3R	Head	Shoulder	Elbow	Wrist	Hip	Knee	Ankle	Mean	Mean@0.1
ResNet-50	256 × 256	-	96.4	95.3	89.0	83.2	88.4	84.0	79.6	88.5	34.0
ResNet-50	256 × 256	$\checkmark$	<b>96.3</b>	<b>95.2</b>	<b>88.8</b>	<b>83.4</b>	<b>88.5</b>	<b>84.3</b>	<b>79.8</b>	<b>88.6</b>	<b>34.9</b>
ResNet-101	256 × 256	-	96.9	95.9	89.5	84.4	88.4	84.5	80.7	89.1	34.0
ResNet-101	256 × 256	$\checkmark$	<b>96.7</b>	<b>96.0</b>	<b>89.3</b>	<b>84.4</b>	<b>88.5</b>	<b>84.3</b>	<b>80.6</b>	<b>89.1</b>	<b>35.0</b>
ResNet-152	256 × 256	-	97.0	95.9	90.0	85.0	89.2	85.3	81.3	89.6	35.0
ResNet-152	256 × 256	$\checkmark$	<b>96.8</b>	<b>95.9</b>	<b>90.1</b>	<b>84.9</b>	<b>89.3</b>	<b>85.3</b>	<b>81.3</b>	<b>89.6</b>	<b>36.2</b>
HRNet-W32	256 × 256	-	97.1	95.9	90.3	86.4	89.1	87.1	83.3	90.3	37.7
HRNet-W32	256 × 256	$\checkmark$	<b>97.1</b>	<b>95.9</b>	<b>90.6</b>	<b>86.2</b>	<b>89.4</b>	<b>86.8</b>	<b>82.9</b>	<b>90.3</b>	<b>39.1</b>
HRNet-W32	256 × 256	$\checkmark\checkmark$	<b>97.1</b>	<b>96.1</b>	<b>90.8</b>	<b>86.1</b>	<b>89.2</b>	<b>86.4</b>	<b>82.6</b>	<b>90.3</b>	<b>39.3</b>

TABLE 12

Results on COCO validation set. In each block, the first row indicates the performance of pretrained model by [22] using the compensation method “shift a quarter to the second maximum activation point”. The second row with  $\checkmark$  indicates the performance when using the proposed method only in inference stage; The third row with  $\checkmark\checkmark$  (if exist) indicates the performance when using the proposed method in both training and inference stages. **GT** indicates testing with the ground truth person bounding boxes.

Backbone	Input	GT	H3R	AP	AP .5	AP .75	AP (M)	AP (L)	AR	AR .5	AR .75	AR (M)	AR (L)
HRNet-W32	256 × 192	-	-	0.744	0.905	0.819	0.708	0.810	0.798	0.942	0.865	0.757	0.858
HRNet-W32	256 × 192	-	$\checkmark$	<b>0.750</b>	<b>0.906</b>	<b>0.820</b>	<b>0.715</b>	<b>0.817</b>	<b>0.802</b>	<b>0.942</b>	<b>0.865</b>	<b>0.761</b>	<b>0.861</b>
HRNet-W32	256 × 192	-	$\checkmark\checkmark$	<b>0.749</b>	<b>0.899</b>	<b>0.814</b>	<b>0.712</b>	<b>0.820</b>	<b>0.801</b>	<b>0.939</b>	<b>0.858</b>	<b>0.758</b>	<b>0.863</b>
HRNet-W32	256 × 192	$\checkmark$	-	0.765	0.935	0.837	0.739	0.808	0.793	0.945	0.858	0.762	0.841
HRNet-W32	256 × 192	$\checkmark$	$\checkmark$	<b>0.773</b>	<b>0.936</b>	<b>0.846</b>	<b>0.746</b>	<b>0.817</b>	<b>0.800</b>	<b>0.947</b>	<b>0.861</b>	<b>0.769</b>	<b>0.848</b>
HRNet-W32	256 × 192	$\checkmark$	$\checkmark\checkmark$	<b>0.775</b>	<b>0.936</b>	<b>0.847</b>	<b>0.744</b>	<b>0.819</b>	<b>0.799</b>	<b>0.941</b>	<b>0.861</b>	<b>0.768</b>	<b>0.847</b>
HRNet-W48	256 × 192	-	-	0.751	0.906	0.822	0.715	0.818	0.804	0.943	0.867	0.762	0.864
HRNet-W48	256 × 192	-	$\checkmark$	<b>0.756</b>	<b>0.906</b>	<b>0.825</b>	<b>0.718</b>	<b>0.825</b>	<b>0.806</b>	<b>0.941</b>	<b>0.868</b>	<b>0.763</b>	<b>0.869</b>
HRNet-W48	256 × 192	$\checkmark$	-	0.771	0.936	0.847	0.741	0.819	0.799	0.945	0.863	0.765	0.851
HRNet-W48	256 × 192	$\checkmark$	$\checkmark$	<b>0.777</b>	<b>0.936</b>	<b>0.848</b>	<b>0.747</b>	<b>0.825</b>	<b>0.804</b>	<b>0.945</b>	<b>0.868</b>	<b>0.771</b>	<b>0.856</b>
HRNet-W32	384 × 288	-	-	0.758	0.906	0.825	0.720	0.827	0.809	0.943	0.869	0.767	0.871
HRNet-W32	384 × 288	-	$\checkmark$	<b>0.762</b>	<b>0.906</b>	<b>0.828</b>	<b>0.722</b>	<b>0.832</b>	<b>0.812</b>	<b>0.943</b>	<b>0.870</b>	<b>0.768</b>	<b>0.874</b>
HRNet-W32	384 × 288	-	$\checkmark\checkmark$	<b>0.762</b>	<b>0.905</b>	<b>0.830</b>	<b>0.725</b>	<b>0.833</b>	<b>0.812</b>	<b>0.942</b>	<b>0.873</b>	<b>0.769</b>	<b>0.874</b>
HRNet-W32	384 × 288	$\checkmark$	-	0.777	0.936	0.847	0.748	0.825	0.804	0.944	0.864	0.770	0.856
HRNet-W32	384 × 288	$\checkmark$	$\checkmark$	<b>0.781</b>	<b>0.936</b>	<b>0.848</b>	<b>0.750</b>	<b>0.831</b>	<b>0.808</b>	<b>0.944</b>	<b>0.865</b>	<b>0.774</b>	<b>0.860</b>
HRNet-W32	384 × 288	$\checkmark$	$\checkmark\checkmark$	<b>0.786</b>	<b>0.936</b>	<b>0.858</b>	<b>0.755</b>	<b>0.834</b>	<b>0.810</b>	<b>0.943</b>	<b>0.871</b>	<b>0.777</b>	<b>0.861</b>
HRNet-W48	384 × 288	-	-	0.763	0.908	0.829	0.723	0.834	0.812	0.942	0.871	0.767	0.876
HRNet-W48	384 × 288	-	$\checkmark$	<b>0.765</b>	<b>0.907</b>	<b>0.829</b>	<b>0.724</b>	<b>0.838</b>	<b>0.814</b>	<b>0.941</b>	<b>0.871</b>	<b>0.769</b>	<b>0.878</b>
HRNet-W48	384 × 288	$\checkmark$	-	0.781	0.936	0.849	0.753	0.831	0.809	0.947	0.867	0.775	0.860
HRNet-W48	384 × 288	$\checkmark$	$\checkmark$	<b>0.785</b>	<b>0.936</b>	<b>0.849</b>	<b>0.757</b>	<b>0.836</b>	<b>0.812</b>	<b>0.945</b>	<b>0.870</b>	<b>0.778</b>	<b>0.864</b>

**Implementation Details.** We use the widely used heatmap regression method for human pose estimation, HRNet [22] as our baseline <sup>3</sup>. Specifically, the proposed method can be easily integrated with typical heatmap regression models and the modifications for the experiments is available <sup>4</sup>. For MPII Human Pose dataset, we use the widely adopted evaluation metric, PCKh@ $\alpha$  [77], with different matching thresholds, i.e.,  $\alpha = 0.5, 0.1$ . A smaller matching threshold, e.g.,  $\alpha = 0.1$  is a more strict evaluation metric for accurate localization. For COCO dataset, we use the standard evaluation metric, averaged precision (AP) and averaged recall (AR), in which the object keypoint similarity (OKS) is used as the similarity measure between ground truth objects and predicted objects [78].

**Results on MPII Human Pose Dataset.** As shown in Table 11, the proposed method achieves comparable performance to the baseline under a coarse evaluation metric,

PCKh@0.5; When using a more accurate evaluation metric, PCKh@0.1, the proposed method then outperforms the baseline with a large margin, e.g., from 35.0 to 36.2 for ResNet-152, and from 37.7 to 39.3 for HRNet-W32.

**Results on COCO Dataset.** As shown in Table 12, the proposed method improves the averaged precision (AP) with a clear margin in different settings. Specifically, we see that 1) the proposed method achieves a larger improvement when using a lower input resolution; and 2) the major improvement on AP comes from the person instances of medium and large size, i.e., AP(M) and AP(L).

When applying the proposed method to semantic landmark localization, it contains only one hyper-parameter  $k$ , i.e., the number of alternative activation points. To better understand the effectiveness of the proposed method for human pose estimation, we perform ablation studies on different numbers of alternative activation points on both MPII and COCO datasets, as shown in Table 13 and Table 14, respectively. Specifically, we find that the proposed method achieves stable performance when  $k$  is between 5 and 25, making it easy to choose a proper  $k$  for validation data.

3. <https://github.com/leoxiaobin/deep-high-resolution-net.pytorch/>

4. <https://github.com/baoshengyu/deep-high-resolution-net.pytorch/>

TABLE 13

Results on MPII validation set. The input resolution is  $256 \times 256$  pixels. The first row indicates the performance when using the compensation method “shift a quarter to the second maximum activation point”.

Backbone	$k$	Head	Shoulder	Elbow	Wrist	Hip	Knee	Ankle	Mean	Mean@0.1
HRNet-W32	-	97.1	95.9	90.3	86.4	89.1	87.1	83.3	90.3	37.7
HRNet-W32	1	97.033	95.703	90.131	86.312	88.402	86.802	82.924	90.055	32.808
HRNet-W32	2	97.033	95.856	90.302	86.416	88.818	87.004	83.325	90.247	35.912
HRNet-W32	3	97.135	95.975	90.302	86.347	89.250	86.741	83.018	90.271	37.668
HRNet-W32	4	97.237	95.907	90.643	86.141	89.164	86.862	83.089	90.294	36.997
HRNet-W32	5	97.203	95.839	90.677	86.141	89.147	87.124	82.994	90.315	38.774
HRNet-W32	6	97.101	95.839	90.677	86.262	89.181	86.923	83.089	90.310	38.548
HRNet-W32	7	97.135	95.822	90.609	86.313	89.199	86.943	83.113	90.312	37.913
HRNet-W32	8	97.033	95.822	90.557	86.175	89.147	86.922	82.876	90.245	38.129
HRNet-W32	9	97.067	95.822	90.694	86.329	89.112	86.942	82.876	90.284	38.457
HRNet-W32	10	97.033	95.873	90.626	86.141	89.372	86.862	82.995	90.297	39.024
HRNet-W32	11	<b>97.101</b>	<b>95.907</b>	<b>90.592</b>	<b>86.244</b>	<b>89.406</b>	<b>86.842</b>	<b>82.853</b>	<b>90.302</b>	<b>39.139</b>
HRNet-W32	12	97.101	95.822	90.660	86.175	89.475	86.761	82.900	90.297	38.996
HRNet-W32	13	97.101	95.822	90.694	86.141	89.475	86.741	82.829	90.289	38.855
HRNet-W32	14	97.033	95.822	90.728	86.141	89.337	86.640	82.806	90.250	38.616
HRNet-W32	15	97.169	95.754	90.609	86.124	89.337	86.801	82.475	90.211	38.798
HRNet-W32	16	97.101	95.771	90.694	86.141	89.199	86.882	82.569	90.226	38.691
HRNet-W32	17	97.067	95.822	90.609	86.142	89.285	86.821	82.617	90.224	<b>39.053</b>
HRNet-W32	18	97.033	95.822	90.626	86.004	89.250	86.801	82.522	90.193	<b>39.048</b>
HRNet-W32	19	97.033	95.839	90.626	85.953	89.250	86.822	82.593	90.198	<b>39.058</b>
HRNet-W32	20	96.999	95.788	90.626	86.039	89.389	86.801	82.664	90.226	39.014
HRNet-W32	21	96.999	95.771	90.677	85.935	89.337	86.862	82.451	90.187	38.855
HRNet-W32	22	96.999	95.856	90.626	86.090	89.268	86.741	82.475	90.198	38.842
HRNet-W32	23	96.999	95.890	90.609	86.038	89.164	86.801	82.499	90.187	39.037
HRNet-W32	24	96.862	95.754	90.592	86.021	89.233	86.842	82.333	90.146	39.089
HRNet-W32	25	96.930	95.754	90.506	86.055	89.302	86.721	82.309	90.135	<b>39.126</b>
HRNet-W32	30	96.862	95.788	90.438	86.004	89.372	86.660	82.144	90.101	38.759
HRNet-W32	35	96.623	95.873	90.523	85.936	89.354	86.701	81.884	90.075	38.964
HRNet-W32	40	96.385	95.856	90.523	85.816	89.406	86.721	81.908	90.049	38.618
HRNet-W32	45	96.317	95.669	90.506	85.746	89.285	86.660	82.026	89.990	38.579
HRNet-W32	50	96.214	95.686	90.506	85.678	89.268	86.439	81.648	89.899	38.584
HRNet-W32	55	96.044	95.669	90.404	85.335	89.337	86.439	81.506	89.815	38.496
HRNet-W32	60	95.805	95.533	90.302	85.147	89.147	86.419	81.270	89.672	38.332
HRNet-W32	65	95.703	95.618	90.251	85.079	89.164	86.419	81.081	89.646	38.218
HRNet-W32	70	95.498	95.584	90.165	85.215	89.302	86.378	80.963	89.633	38.197
HRNet-W32	75	95.259	95.533	90.029	85.147	89.147	86.318	80.467	89.487	38.054
HRNet-W32	80	95.020	95.516	90.046	84.907	89.216	86.197	80.255	89.404	37.684
HRNet-W32	85	94.679	95.465	89.927	84.925	89.337	86.258	80.042	89.357	37.463
HRNet-W32	90	94.407	95.431	89.790	84.907	89.233	86.197	79.735	89.251	37.208
HRNet-W32	95	94.065	95.414	89.773	84.890	89.302	86.097	79.263	89.165	36.719
HRNet-W32	100	93.827	95.482	89.603	84.737	89.320	86.076	78.578	89.032	36.180
HRNet-W32	105	93.520	95.448	89.603	84.599	89.199	85.996	77.964	88.884	35.532
HRNet-W32	110	93.008	95.448	89.518	84.273	89.147	85.835	77.114	88.657	34.770
HRNet-W32	115	92.565	95.296	89.501	84.085	89.112	85.794	76.405	88.483	33.352
HRNet-W32	120	92.121	95.262	89.398	83.930	89.060	85.533	75.272	88.238	31.814
HRNet-W32	125	91.473	95.160	89.160	83.554	88.991	85.472	74.162	87.939	30.065
HRNet-W32	130	90.825	94.939	89.211	83.023	89.095	85.089	72.910	87.609	27.528
HRNet-W32	135	90.246	94.667	89.006	82.577	88.852	84.807	71.209	87.164	24.757
HRNet-W32	140	89.529	94.463	88.853	82.046	88.679	83.800	69.792	86.659	21.788
HRNet-W32	145	88.404	94.124	88.717	81.310	88.645	82.773	67.997	86.053	19.136
HRNet-W32	150	87.756	93.886	88.614	80.146	88.575	81.383	66.084	85.373	16.586
HRNet-W32	175	82.401	90.829	86.927	71.515	86.014	70.504	56.826	80.109	9.204
HRNet-W32	200	68.008	87.075	82.325	62.146	79.176	58.737	41.120	72.009	5.988

TABLE 14

Results on COCO validation set. The input resolution is  $256 \times 192$  pixels. The first row indicates the performance when using the compensation method “shift a quarter to the second maximum activation point”.

Backbone	$k$	AP	Ap .5	AP .75	AP (M)	AP (L)	AR	AR .5	AR .75	AR (M)	AR (L)
HRNet-W32	-	0.744	0.905	0.819	0.708	0.810	0.798	0.942	0.865	0.757	0.858
HRNet-W32	1	0.723	0.904	0.811	0.690	0.788	0.782	0.941	0.859	0.741	0.841
HRNet-W32	2	0.738	0.905	0.817	0.702	0.805	0.793	0.942	0.864	0.752	0.854
HRNet-W32	3	0.743	0.905	0.819	0.708	0.810	0.797	0.942	0.865	0.756	0.857
HRNet-W32	4	0.743	0.904	0.819	0.709	0.809	0.797	0.941	0.866	0.756	0.857
HRNet-W32	5	0.747	0.904	0.819	0.712	0.814	0.800	0.940	0.866	0.759	0.859
HRNet-W32	6	0.747	0.905	0.820	0.711	0.814	0.799	0.941	0.865	0.759	0.859
HRNet-W32	7	0.745	0.905	0.820	0.709	0.812	0.798	0.941	0.864	0.757	0.857
HRNet-W32	8	0.746	0.905	0.819	0.711	0.813	0.799	0.942	0.863	0.759	0.858
HRNet-W32	9	0.746	0.905	0.819	0.710	0.812	0.798	0.942	0.863	0.758	0.857
HRNet-W32	10	0.749	0.905	0.820	0.713	0.815	0.801	0.943	0.864	0.760	0.860
HRNet-W32	11	<b>0.750</b>	<b>0.906</b>	<b>0.820</b>	<b>0.715</b>	<b>0.817</b>	<b>0.802</b>	<b>0.942</b>	<b>0.865</b>	<b>0.761</b>	<b>0.861</b>
HRNet-W32	12	0.750	0.906	0.821	0.714	0.817	0.801	0.942	0.865	0.760	0.861
HRNet-W32	13	0.749	0.906	0.821	0.713	0.816	0.800	0.942	0.865	0.760	0.860
HRNet-W32	14	0.749	0.905	0.820	0.713	0.816	0.800	0.941	0.864	0.760	0.860
HRNet-W32	15	0.749	0.906	0.820	0.713	0.817	0.800	0.942	0.863	0.760	0.860
HRNet-W32	16	0.749	0.905	0.820	0.713	0.816	0.800	0.941	0.863	0.760	0.860
HRNet-W32	17	0.750	0.905	0.821	0.714	0.817	0.801	0.942	0.863	0.761	0.860
HRNet-W32	18	0.750	0.905	0.820	0.713	0.817	0.801	0.942	0.864	0.760	0.860
HRNet-W32	19	0.750	0.904	0.820	0.714	0.816	0.801	0.941	0.864	0.760	0.860
HRNet-W32	20	0.749	0.904	0.820	0.713	0.816	0.800	0.940	0.864	0.760	0.859
HRNet-W32	21	0.747	0.904	0.819	0.712	0.813	0.799	0.940	0.862	0.758	0.858
HRNet-W32	22	0.749	0.904	0.819	0.713	0.815	0.799	0.941	0.863	0.759	0.859
HRNet-W32	23	0.749	0.904	0.819	0.713	0.816	0.800	0.941	0.863	0.760	0.860
HRNet-W32	24	0.749	0.904	0.820	0.713	0.817	0.800	0.941	0.863	0.759	0.860
HRNet-W32	25	0.749	0.905	0.820	0.713	0.817	0.800	0.941	0.864	0.760	0.860
HRNet-W32	30	0.749	0.905	0.819	0.714	0.818	0.800	0.941	0.862	0.759	0.859
HRNet-W32	35	0.748	0.902	0.819	0.712	0.816	0.799	0.940	0.862	0.758	0.859
HRNet-W32	40	0.746	0.901	0.818	0.710	0.814	0.797	0.939	0.861	0.756	0.857
HRNet-W32	45	0.746	0.901	0.815	0.710	0.814	0.796	0.939	0.860	0.755	0.857
HRNet-W32	50	0.746	0.901	0.814	0.710	0.816	0.797	0.938	0.859	0.755	0.857
HRNet-W32	75	0.741	0.899	0.811	0.705	0.810	0.792	0.936	0.856	0.751	0.853
HRNet-W32	100	0.734	0.897	0.805	0.697	0.803	0.785	0.934	0.850	0.743	0.846
HRNet-W32	125	0.717	0.893	0.795	0.682	0.785	0.770	0.930	0.841	0.727	0.831
HRNet-W32	150	0.651	0.889	0.755	0.629	0.702	0.713	0.925	0.809	0.680	0.762